Toward numerical-relativity informed effective-one-body waveforms for dynamical capture black hole binaries

Tomas Andrade,[1] Juan Trenado,[1] Simone Albanesi,[2,3] Rossella Gamba,[4] Sebastiano Bernuzzi,[4] Alessandro Nagar,[3,5] Juan Calderon Bustillo,[6,7] Nicolas Sanchis-Gual,[8] José A. Font,[8,9] William Cook,[4] Boris Daszuta,[4] Francesco Zappa,[4] and David Radice[10,11,12]

[1]*Departament de Física Quàntica i Astrofísica, Institut de Ciències del Cosmos, Universitat de Barcelona, Martí i Franquès 1, E-08028 Barcelona, Spain*
[2]*Dipartimento di Fisica, Università di Torino, via P. Giuria 1, 10125 Torino, Italy*
[3]*INFN Sezione di Torino, Via P. Giuria 1, 10125 Torino, Italy*
[4]*Theoretisch-Physikalisches Institut, Friedrich-Schiller-Universität Jena, 07743, Jena, Germany*
[5]*Institut des Hautes Etudes Scientifiques, 91440 Bures-sur-Yvette, France*
[6]*Instituto Galego de Física de Altas Enerxías, Universidade de Santiago de Compostela, 15782 Santiago de Compostela, Galicia, Spain*
[7]*Department of Physics, The Chinese University of Hong Kong, Shatin, N.T., Hong Kong*
[8]*Departamento de Astronomía y Astrofísica, Universitat de València, Dr. Moliner 50, 46100 Burjassot (València), Spain*
[9]*Observatori Astronòmic, Universitat de València, Catedrático José Beltrán 2, 46980 Paterna (València), Spain*
[10]*Institute for Gravitation and the Cosmos, The Pennsylvania State University, University Park, Pennsylvania 16802, USA*
[11]*Department of Physics, The Pennsylvania State University, University Park, Pennsylvania 16802, USA*
[12]*Department of Astronomy and Astrophysics, The Pennsylvania State University, University Park, Pennsylvania 16802, USA*

(Received 14 February 2024; accepted 15 March 2024; published 12 April 2024)

Dynamical captures of black holes may take place in dense stellar media due to the emission of gravitational radiation during a close passage. Detection of such events requires detailed modeling, since their phenomenology qualitatively differs from that of quasicircular binaries. Very few models can deliver such waveforms, and none includes information from numerical relativity (NR) simulations of non-quasicircular coalescences. In this study we present a first step towards a fully NR-informed effective-one-body (EOB) model of dynamical captures. We perform 14 new simulations of single and double encounter mergers, and use this data to inform the merger-ringdown model of the `TEOBResumS-Dalì` approximant. We keep the initial energy approximately fixed to the binary mass, and vary the mass-rescaled, dimensionless angular momentum in the range (0.6, 1.1), the mass ratio in (1, 2.15), and aligned dimensionless spins in $(-0.5, 0.5)$. We find that the model is able to match NR to 97%, improving previous performances, without the need of modifying the baseline template. Upon NR informing the model, this improves to 99% with the exception of one outlier corresponding to a direct plunge. The maximum EOB/NR phase difference at merger for the uninformed model is of 0.15 radians, which is reduced to 0.1 radians after the NR information is introduced. We outline the steps towards a fully informed EOB model of dynamical captures, and discuss future improvements.

DOI: 10.1103/PhysRevD.109.084025

I. INTRODUCTION

The detection and characterization of gravitational waves (GWs) requires a multidisciplinary effort that combines instruments of exquisite precision—the LIGO-Virgo-KAGRA (LVK) network of interferometers [1–3]—and sophisticated data analysis techniques. Thus far, the most numerous events in the LVK catalog have been categorized as binary black holes (BBHs) with small or negligible eccentricity [4]. This type of event is expected to ensue from stellar binaries that have evolved in isolation from their environments and have radiated away their excess angular momentum, thus displaying quasicircular orbits once they enter the sensitive band. However, some events do not easily fit in this category. In particular, the most massive BBH observed to date, GW190521 [5,6], has been shown to be consistent with a dynamical capture of two nonspinning black holes [7]. Alternative interpretations of this source are discussed in [8–11].

 © 2024 American Physical Society

Dynamical captures may take place in dense stellar media such as globular clusters if the individual black holes radiate gravitational energy during a close passage [12,13]. Since the phenomenology of these events is sensibly different from the quasicircular ones [14–16], detailed modeling of the waveforms is required to detect and properly characterize such events through matched filtering. Indeed, if quasicircular templates are used for the search and analysis of waveforms generated by dynamical captures, the events might be missed or incorrectly analyzed [16–18]. Moreover, events of this kind can be detected for farther and heavier black hole systems [19]. Dynamical captures are also relevant for next-generation detectors such as LISA [20] and the Einstein Telescope [21]. The detectability rate for next-generation, ground-based detectors has been estimated in Ref. [22].

Numerical relativity (NR), i.e. the fully fledged evolution of Einstein's equations, provides the most detailed description of BBH mergers. However, a systematic NR study of dynamical captures is presently missing. Low energy nonspinning encounters have been systematically studied by Gold and Brügmann [23]. Fewer initial data including spin and mass ratio effects have been considered in Refs. [7,17,24,25]. NR simulations for hyperbolic encounters have also been recently considered in [26] including spin and varying mass ratios. Several new simulations of bound orbits but with large eccentricity and precessing spins have also been recently reported [10,27]. The computational cost involved in spanning the possible orbital configurations for different binaries (mass ratio and spins) makes it impractical to directly employ NR for a complete survey and for constructing waveform approximants. Similarly to the circularized orbits case, our strategy is to exploit synergy with analytical relativity.

Reference Nagar et al. [16] proposed the first analytical and complete general-relativistic description of the dynamics and waveforms of dynamical captures. The approach of Nagar et al. [16] is based on the effective-one-body (EOB) framework `TEOBResumS` [28–34] and in particular on the generic orbits version `TEOBResumS-Dalì` [35–37]. This model was the basis for the analysis of GW190521 reported by [7], as well as the eccentric analyses presented in [38]. It produces quantitative predictions for the waveform from the entire orbital parameter space, including spin and mass-ratio effects. Remarkably, despite not being informed by any eccentric NR simulation, `TEOBResumS-Dalì` shows mismatches below 1% for almost all of the available mildly eccentric configurations of the Simulating eXtreme Spacetimes catalog [36] as well as for the Rochester Institute of Technology catalog [7]. The accuracy of the EOB dynamics has been also tested in the hyperbolic encounter scenario by comparing the EOB/NR scattering angles for both nonspinning and spinning configurations [39–41]. Moreover, the accuracy of the fluxes, i.e. the nonconservative part of the dynamics, has been tested both for comparable mass and high-mass ratio systems [42–44] in the quasicircular case, and for hyperbolic and eccentric systems with extreme mass ratio [45,46]. However, even if a few EOB/NR comparisons for equal mass binaries have been reported in the supplemental material of Ref. [7], the dynamical capture scenario for comparable mass black holes still needs to be explored in detail. A search for hyperbolic encounters using public data was carried out in [47], with results consistent with the false alarm search rate. Observational implications of dynamical captures have recently been considered in [48].

The main goal of this work is to assess the capabilities of the latest version of `TEOBResumS-Dalì` [36] in the dynamical capture scenario. We carry out a series of new NR simulations of highly eccentric bounded orbits, which, as we argue below, can be interpreted as the late stages of dynamical captures. This allows us to quantitatively verify some of the key predictions of Nagar et al. [16], and propose a first strategy to inform the model with NR data. As we show below, we find that by appropriately informing our model with data coming from NR simulations we are able to obtain waveforms more than 99% faithful to NR in most cases.

This paper is organized as follows: In Sec. II we present our new NR simulations and perform the first comparison between the Einstein Toolkit and GR-Athena++ NR codes. We describe in some detail the configurations chosen, the two codes employed to obtain them, and the tests that we performed to ensure convergence. We also discuss the postprocessing of the NR data, with a focus on waveform extraction techniques. In Sec. III we briefly introduce the `TEOBResumS-Dalì` model, discuss the NR-informed parameters that we consider, and tackle the issue of connecting NR and EOB initial data. In Sec. IV we perform comparisons between our simulations and `TEOBResumS-Dalì`, presenting both time-domain phasing comparisons and mismatch computations. Finally, in Sec. V we summarize and discuss our results. Geometric units with $G = c = 1$ are employed throughout the text, unless otherwise specified.

II. NUMERICAL RELATIVITY SIMULATIONS

A. Numerical codes

1. Einstein Toolkit

For the bulk of this work we use the open source software Einstein Toolkit [49]. This code is organized as a main driver (Cactus) and a series of modules (thorns) that perform specific tasks. BBH initial data are computed with the TwoPunctures thorn [50,51], which is appropriate to solve the constraint equations on the initial $t = 0$ slice for the modest values of spins and mass ratio considered in this work. In the range of parameters we have explored, this algorithm converges to the desired numerical precision within a few iterations. The time evolution is carried out by the MLBSSN thorn which implements the Baumgarte-Shapiro-Shibata-Nakamura formulation of vacuum general relativity [52,53]. We use sixth order finite differences for spatial derivatives and a method-of-lines time integration with a fourth order Runge-Kutta scheme. Moreover, we include Kreiss-Oliger dissipation of order 9 scaled with a factor of $\epsilon = 0.1$. The Courant-Friedrichs-Lewy factor for our Einstein Toolkit runs is 0.1.

Our grid setup consists of a cubic box of edge $L = 640M$ (in the coarsest level, the Cartesian coordinates range from $-320M$ to $320M$) and spacing at the coarsest level $\delta x = \{3, 4, 6\}M$, corresponding to (low, medium, high) resolutions. Here M is the total mass of the binary, defined as the sum of the individual Arnowitt-Deser-Misner (ADM) masses. We have carried out most of our simulations at $\delta x = 4M$. We also provide convergence tests for selected simulations considering the low and high resolutions. The code uses Berger-Oliger mesh refinement with nine overlapping refinement levels in a box-in-box fashion, with the two most refined boxes containing the two punctures. The boxes follow the two punctures, whose position is determined during the evolution with the PunctureTracker thorn. This setting results in a puncture resolution of $\delta x_p = 4/2^8 M = 0.015625M$. For unequal masses, we add an extra refinement level only at the smaller black hole. This was proven crucial to obtain robust results as we vary resolution. We exploit the reflection symmetry of our configurations to reduce the computational domain by a half in the z direction.

We extract the wave content of our simulations using the thorns WeylScal4 and Multipole which output the Weyl scalars ψ_4 expanded in spherical harmonics up to $\ell = 8$, at fixed radius. We check that $R\psi_4 = \text{const}$, as expected for the extraction radii $R = \{70, 80, 90, 100, 110\}M$, which are located in a refinement level at the same resolution $\delta x = 4/2^2 M = 1M$. On the contrary, extraction radii $R \geq 120$ fall within levels of lower resolution, which causes power loss due to numerical dissipation.

2. GR-Athena++

In this work we also extend the set of GR-Athena++ [54] simulations presented in [7]. The initial data are computed with a stand-alone version of the thorn TwoPunctures [50,51]. The time evolution is then performed by GR-Athena++ using the Z4c formulation [55]. Moving puncture gauge conditions with the same parameters in Ref. [54] are adopted. As in the Einstein Toolkit case, we use sixth order finite-difference methods for the spatial derivatives and we perform the time integration using a fourth order Runge-Kutta algorithm. In contrast, for the simulations performed here, Kreiss-Oliger dissipation of order 8 is included with a factor $\epsilon = 0.02$. We also choose a bigger box with edge $L = 3072M$, so that in the coarsest level the Cartesian coordinates range from $-1536M$ to $1536M$. The adaptive mesh refinement (AMR) in GR-Athena++ is oct-tree based, with the grid organized as an initial Mesh divided into Meshblocks which have all the same number of grid points but (possibly) different physical size. For a cubic initial Mesh and cubic Meshblocks, the grid setup in GR-Athena++ is regulated by three parameters: the number of grid points in the edges of the unrefined initial mesh N_M, the number of grid points in the edges of Meshblocks N_B, and the number of physical refinement levels N_L. The grid structure is ultimately determined by an AMR criterion, which, when satisfied, (de)refines a given MeshBlock, resulting in a (larger) smaller block with (half) double the resolution. For BBH simulations the AMR criterion used mimics the box-in-box strategy mentioned above. In our simulations we consider $N_B = 16$, $N_L = 11$, and $N_M = \{128, 192, 256\}$. These values are chosen so that the resolution at the punctures is the same as the simulations performed with the Einstein Toolkit code. For all the runs we consider a Courant-Friedrichs-Lewy number of 0.5. The Weyl scalar is then extracted at $R = \{80, 90, 100, 110, 120, 130, 140\}M$ using an approximate geodesic sphere built using 9002 vertices. For the three grids considered, the resolutions in the extraction zones at the merger time are $\delta x_R = \{3, 2, 1.5\}M$ for $R > 96M$, while they are $\delta x_R = \{1.5, 1, 0.75\}M$ for $48M < R < 96M$. Note that at the beginning of the simulation the extraction zone for $R > 96M$ does not have a uniform resolution since the positions of the two punctures make some portions of the zone more refined. We observed that $R\psi_4$ remains approximately constant at all the extraction radii, showing that ψ_4 scales as $1/R$, as expected. More technical details on the structure of the grid and of the geodesic sphere can be found in Ref. [54]. Note that no grid symmetries are employed for these runs.

B. Initial data

We consider initial data consisting of two black holes of (quasilocal) ADM masses M_1 and M_2 separated by a coordinate distance D. The total mass of the binary is $M = M_1 + M_2$. We take their ADM linear momenta to be $\vec{P}_1 = -\vec{P}_2$, with $\vec{P}_1 = P_{qc}(\cos\theta, \sin\theta, 0)$, where P_{qc} corresponds to the quasicircular value. The black holes have spins $\vec{J}_1$, $\vec{J}_2$ aligned with the orbital angular momenta, so that $\vec{J}_1 = \chi_1 M_1^2(0, 0, 1)$, $\vec{J}_2 = \chi_2 M_2^2(0, 0, 1)$. Here $\chi_{1,2}$ are dimensionless spin parameters. Following [23] we take $D = 20M$ which in turn implies $P_{qc} = 0.06175M$. See Fig. 1 for a schematic depiction of our initial data.

C. Simulation results

We considered 14 configurations that were simulated using Einstein Toolkit. Table I collects the initial physical parameters, while in Appendix A we show the puncture trajectories and the time evolution of the $\ell = m = 2$ multipole of the Weyl scalar ψ_4. Simulations will be refereed to using their ID as defined in the first column of Table I. The phenomenology of the transition from eccentric inspiral, zoom-whirl behavior, and dynamical capture was studied in Refs. [23,56] as the initial angle

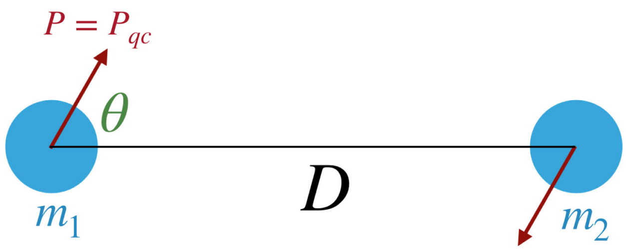

FIG. 1. Schematic depiction of our initial data. The initial separation D and the value of P are kept fixed at $20M$ and $0.06175M$, respectively, and we vary the initial angle θ as well as the intrinsic spins of the BH components.

θ is varied. For angles close to $\theta = 0$ (head-on collision), one has direct plunges. For fixed values of the initial separation D, one can have various close encounters (including zoom-whirl behavior) before the final merger. Finally, for angles θ beyond a certain threshold, the black hole does not merge. In our set of simulations, for equal masses and θ below 48 degrees we find plunges, in `ETK37q1s0, 42q1s0, 44q1s0, 46q1s0`, while `ETK48q1s0` begins to display features of a zoom whirl which can be fully appreciated in `ETK50q1s0`. Simulations `ETK42q1s0, 48q1s0, 50q1s0` correspond to some of the configurations presented in Ref. [23]. We find good qualitative and quantitative agreement between puncture tracks and waveforms. These are a plunge, a transition to double encounter, and a double encounter, respectively. Note that this agreement is particularly nontrivial for `ETK48q1s0`, since, due to the fact that this is a boundary case between single and double encounters, slight changes on the initial data or resolution can lead to different results. We further analyze these three cases by performing self-convergence tests and a code comparison between Einstein Toolkit and GR-Athena++, see Sec. II G.

As also stated in [23], varying the mass ratio can also result in zoom whirls. We explore this regime in our series `ETK42, 42q150, 42q200, ETK42q2.15s0`, going from a plunge to a fully developed zoom whirl. Moreover, we have observed that zoom whirls can be induced by increasing the angular momenta by adding spin to the components of a binary which yields a plunge orbit in the nonspinning case. This is found in our simulations `ETK42q1s050-, 42q1s025-, 42q1s0, 42q1s025++, 42q1s050++` as discussed in Sec. IV A 2 and is analytically explained via the spin-orbit interaction. NR simulations are also known to suffer from "junk radiation," i.e. radiation caused by the underlying conformally flat assumption used for the computation of the initial data. In our case, we observe a small burst of radiation in ψ_4 which arrives at the extraction radius R at a time $t_{\rm junk} \sim R$. We discuss in more detail the impact of junk radiation on our simulations in Sec. II E below.

We observe in Table I that all of our NR simulations have ADM energies which are slightly lower than M. Therefore, strictly speaking, these are high eccentricity *bounded* configurations. However, as we show in Appendix D, it is possible to interpret them as the late stages of initially unbounded configurations, hence describing the phenomenology of dynamical captures.

TABLE I. Dynamical capture BBH configurations considered in this work. From left to right the columns report: the configuration name; the mass ratio $q = m_1/m_2$, the angle θ of the component of the tangential momentum, the dimensionless spins $\chi_i \equiv S_i/m_i^2$, the initial ADM energy and angular momentum $(E_0^{\rm ADM}, J_0^{\rm ADM})$, the final energy and angular momentum (E_f, J_f), and the gravitational wave losses $(\Delta E, \Delta J)$, all expressed in units of the total mass M. The initial separation is $D = 20M$ for all configurations. All configurations are simulated using the Einstein Toolkit; those marked with a star also with the GR-Athena++ code. See Table II below for additional information.

No.	ID	q	θ [deg]	χ_1	χ_2	$E_0^{\rm ADM}/M$	$J_0^{\rm ADM}/M^2$	E_f/M	J_f/M^2	$\Delta E_{\rm EOB}/M$	$\Delta J_{\rm EOB}/M^2$
1	`ETK37q1s0`	1.00	37	0.00	0.00	0.99427	0.74321	0.97812	0.65522	0.00000	0.00446
2	`ETK42q1s0*`	1.00	42	0.00	0.00	0.99427	0.82634	0.96521	0.67555	0.00005	0.00488
3	`ETK44q1s0`	1.00	44	0.00	0.00	0.99428	0.85786	0.95755	0.66749	0.00000	0.00515
4	`ETK46q1s0`	1.00	46	0.00	0.00	0.99428	0.88834	0.94903	0.64455	0.00008	0.00486
5	`ETK48q1s0*`	1.00	48	0.00	0.00	0.99428	0.91774	0.95035	0.60959	0.00009	0.00539
6	`ETK50q1s0*`	1.00	50	0.00	0.00	0.99429	0.94602	0.94858	0.62682	0.00025	0.00094
7	`ETK42q1s025-`	1.00	42	−0.25	−0.25	0.99425	0.70134	0.97564	0.59586	0.00000	0.00421
8	`ETK42q1s025++`	1.00	42	0.25	0.25	0.99433	0.95134	0.94320	0.70570	0.00000	0.00571
9	`ETK42q1s050-`	1.00	42	−0.50	−0.50	0.99439	0.57634	0.98122	0.49612	0.00000	0.00346
10	`ETK42q1s050++`	1.00	42	0.50	0.50	0.99454	1.07634	0.93980	0.73469	0.00016	0.00606
11	`ETK42q1s050+-`	1.00	42	0.50	−0.50	0.99447	0.82634	0.96517	0.67477	0.00000	0.00496
12	`ETK42q1.5s0`	1.50	42	0.00	0.00	0.99501	0.82634	0.96229	0.65471	0.00000	0.00496
13	`ETK42q2s0`	2.00	42	0.00	0.00	0.99641	0.82634	0.95710	0.58005	0.00079	0.00444
14	`ETK42q2.15s0`	2.15	42	0.00	0.00	0.99687	0.82634	0.96340	0.58504	0.00012	0.00180

D. Postprocessing

The Weyl scalar $\psi_4^{\ell m}$ that is given in output in the numerical simulations that we consider is extracted at a finite radius R and thus needs to be extrapolated at infinity. In this work we consider the extrapolation proposed in Refs. [57,58],

$$\lim_{r\to\infty} r\psi_4^{\ell m} \simeq A\left(r\psi_4^{\ell m} - \frac{(\ell-1)(\ell+2)}{2r}\int dt r\psi_4^{\ell m}\right), \quad (1)$$

where $A = 1–2M/r$ and $r = R(1 + M/(2R))^2$. The plus and cross polarizations of the strain can be expanded in spin-weighted harmonics as

$$h_+(\Omega, t) - ih_\times(\Omega, t) = \frac{1}{R}\sum_{\ell m} {}_{-2}Y_{\ell m}(\Omega)h_{\ell m}(t), \quad (2)$$

where Ω is the angular dependence. The corresponding waveform and fluxes can be obtained from the extrapolated scalar since

$$R\psi_4^{\ell m} = \ddot{h}_{\ell m}. \quad (3)$$

It is well known that performing this double time integration is subtle due to the presence of numerical noise which induces drifts in the signal [59]. Note, moreover, that the algorithm in (1) requires an additional integral, so extraction of the extrapolated strain modes takes three integrals in total. In the case of circularized binaries, it is well established that the most reliable procedure to follow is the fixed-frequency integration (FFI), where the integration is performed in the frequency-domain and a frequency cutoff ω_0 is introduced to get rid of the unphysical features [59]. In that case, since the orbits are quasicircular, the frequency of the emitted gravitational waves is a monotonic increasing function of the time, and therefore it is straightforward to identify the value of ω_0. However, in the case of noncircularized binaries, and in particular for dynamical capture, it is not clear how to identify the cutoff. In particular, we observe that for choices of cutoffs which are large enough to remove the drift in the ringdown, FFI integration makes the amplitude of the precursor unphysically small. To overcome this issue, we use a time-domain integration and then remove the drift in the resulting signals.

For the leading (2,2) modes, after each time integration [including the one in (1)] we remove a complex constant by fitting a zeroth order polynomial in a $100M$ interval after the maximum of ψ_4. For higher modes, the noisier signals require a more elaborate subtraction. In this case, the first integrals of ψ_4 when treated as above present a small drift, which is significantly amplified by performing the second integral. We eliminate the drift from the final signal by performing a fifth order polynomial fit extracted from the whole signal after junk radiation has finalized.

We obtain the strain modes by extracting ψ_4 at $R = 100M$, extrapolating to infinity with (1) and computing the double time integral using direct time integration and subtracting the drift as explained above. We have observed that extrapolation in conjunction with direct time integration can be delicate for some signals and extraction radii. Our choice of extraction at $R = 100M$ is the one that appears most robust.

When visualizing our signals in the time domain we will employ the retarded time $t - r_*$, with r_* the tortoise coordinate

$$r_* = R + 2M\log[R/(2M) - 1], \quad (4)$$

with R the extraction radius and M the sum of the individual ADM masses.

We display the results of our postprocessed waveforms for `ETK42q1s0, 50q1s0` in Fig. 2. We write the modes of the strain in terms of the amplitude and phase as

$$h_{\ell m}(t) = A_{\ell m}(t)e^{i\phi_{\ell m}(t)}, \quad (5)$$

and introduce the difference between Einstein Toolkit and GR-Athena++ results by

$$\Delta A_{22}^{\mathrm{GRAETK}} \coloneqq A_{22}^{\mathrm{GRA}} - A_{22}^{\mathrm{ETK}},$$
$$\Delta\phi_{22}^{\mathrm{GRAETK}} \coloneqq \phi_{22}^{\mathrm{GRA}} - \phi_{22}^{\mathrm{ETK}}. \quad (6)$$

E. Energetics

We compute the radiated energy and angular momentum as a function of time, as (see e.g. [60])

$$\dot{E} = \frac{1}{16\pi}\sum_{(\ell,m)} \dot{h}_{\ell m}\dot{h}^*_{\ell m}, \quad (7)$$

$$\dot{J} = \frac{1}{16\pi}\sum_{(\ell,m)} m\Im[h_{\ell m}\dot{h}^*_{\ell m}]. \quad (8)$$

Note that here we are formally extrapolating to infinity by using the formula (1). Our data includes modes with $2 \le l \le 8$ and $m = -\ell\ldots\ell$, so in practice the sums are limited to these values. We have found that the modes $m = 0$ are numerically noisy so do not include them in the computation. Integrating the fluxes $\dot{E}$, $\dot{J}$ over time, we obtain the total radiated energy and angular momentum. This allows us to define the energy and angular momentum as a function of time t:

$$\mathcal{E}(t) = E_i^{\mathrm{ADM}} - \int_t^\infty dt' \dot{E}(t'), \quad (9)$$

$$\mathcal{J}(t) = J_i^{\mathrm{ADM}} - \int_t^\infty dt' \dot{J}(t'), \quad (10)$$

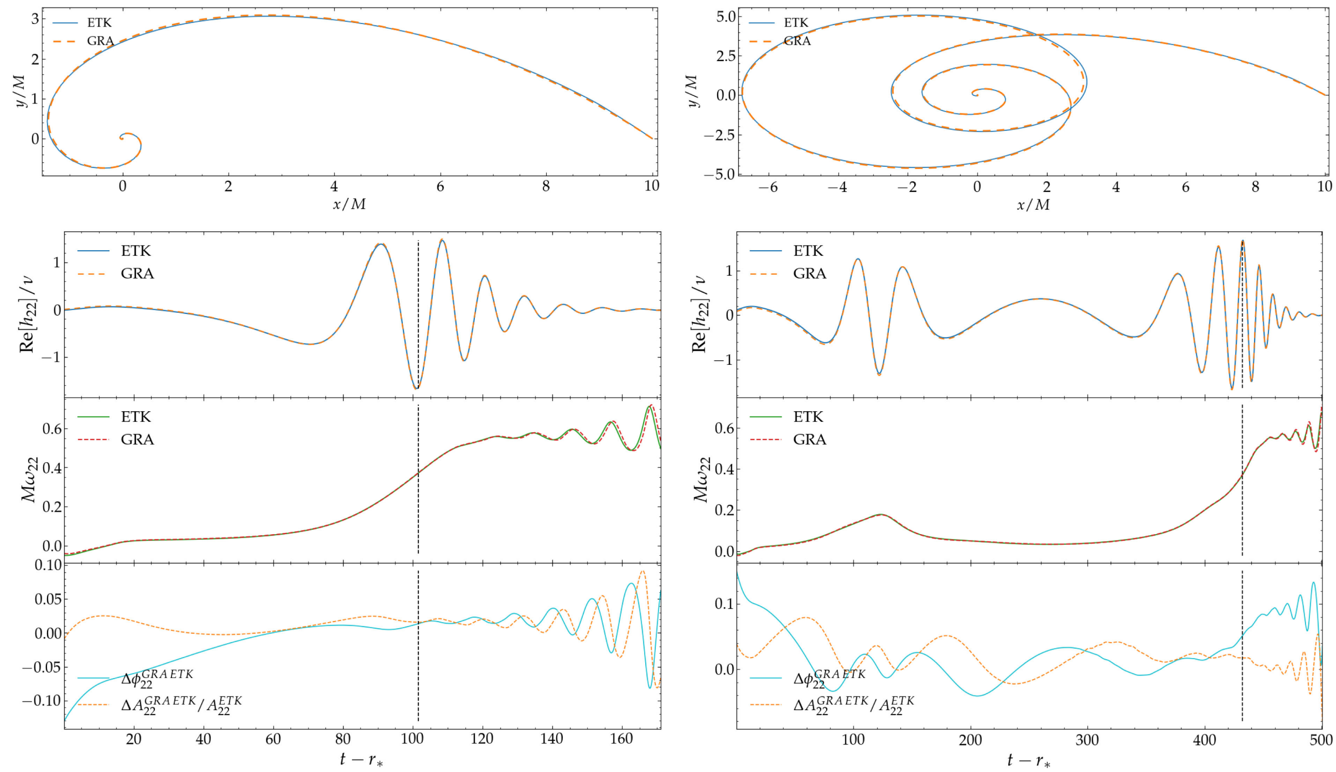

FIG. 2. Example orbit, waveforms, frequency, and amplitude and phase difference, for a direct capture (`ETK42q1s0`, `GRA42q1s0`, left panel) and zoom whirl (`ETK50q1s0`, `GRA50q1s0`, right panel). The differences are defined in (6). We only show the trajectories of one of the black holes to ease visualization. Since these are equal-mass simulations, the other trajectory can be obtained by reflection symmetry. In the direct capture case, the black holes plunge almost immediately, without completing a full orbital cycle. Therefore, the waveform is dominated by merger and ringdown. Conversely, in the zoom-whirl scenario, the bodies undergo multiple encounters before merging, each close passage corresponds to a GW burst. In our code comparison, there is no alignment applied to the waveforms. We show the merger time as a vertical dashed on bottom panels.

where E_i^{ADM}, J_i^{ADM} are the initial ADM total energy and angular momentum of the system as shown in Table I. Following [61], we define the dimensionless binding energy and dimensionless angular momentum as

$$E_b(t) = \frac{\mathcal{E}(t) - M}{\mu}, \tag{11}$$

$$j(t) = \frac{\mathcal{J}(t)}{M\mu}, \tag{12}$$

where $M = m_1 + m_2$ is the sum of the individual initial ADM masses and $\mu = m_1 m_2/M$.

Energetics are a meaningful and robust tool to compare NR data to EOB, e.g. [60–63]. In the case of quasicircular orbits, the NR initial puncture parameters can be constructed to match the 3PN prediction. When junk radiation is correctly taken into account, the initial evolution drives the binary very close to the EOB curve, which is more bound than the 3PN curve [60]. We observe in our dynamical capture scenario that the initial burst of junk radiation has a smaller impact on the energetics with respect to the quasicircular case. However, other sources of inaccuracies like residual gauge ambiguities in the determination of the puncture parameters from the EOB energetics and the reconstruction of the strain from ψ_4 can play a role. Overall, we observe these effects are sufficiently small that the EOB/NR agreement is within the NR errors in the early phase of the dynamics. However, in some cases we allow for a small (less than 1%) adjustment in the ADM quantities to obtain EOB waveforms that best match the NR simulations. These corrections are then also employed when we compare the energy curves between EOB and NR.

F. Faithfulness

The faithfulness (or match) is a common measure to quantify the global difference between two waveforms. For two signals in the time domain $h_1(t)$, $h_2(t)$ the match is defined as

$$\mathcal{F} = \frac{\langle h_1, h_2\rangle}{\sqrt{\langle h_2, h_2\rangle\langle h_1, h_1\rangle}}, \tag{13}$$

where the inner product, assuming a noise function $S_n(f)$, is defined as

TABLE II. Technical information for simulations ETK42q1s0, 48q1s0, 50q1s0 and GRA42q1s0, 48q1s0, 50q1s0. We have runs at low (L), medium (M), and high (H) resolutions for each case. The quantities shown are: coarsest level resolution for Einstein Toolkit (δx), number of grid points at the edges of the coarsest level for GR-Athena++ (N_M), resolution at extraction radius (δx_R), resolution at puncture (δx_p), total simulation time t_{end}, and number of CPUs used. The number of points on the spherical grid where extraction is performed is 3200 for Einstein Toolkit simulations and 9002 for GR-Athena++ ($n_Q = 30$). Note in particular that the puncture resolution δx_p matches for the corresponding resolutions in each code. All physical quantities are measured in units of M.

ID	Res	δx	N_M	δx_R	$\delta x_p\,[10^{-2}]$	t_{end}	CPUs
ETK42q1s0	L	6	⋯	1.5	2.3438	320	180
	M	4	⋯	1.0	1.5625	320	288
	H	3	⋯	0.75	1.1719	320	288
ETK48q1s0	L	6	⋯	1.5	2.3438	450	180
	M	4	⋯	1.0	1.5625	450	288
	H	3	⋯	0.75	1.1719	450	288
ETK50q1s0	L	6	⋯	1.5	2.3438	750	180
	M	4	⋯	1.0	1.5625	750	288
	H	3	⋯	0.75	1.1719	750	288
GRA42q1s0	L	⋯	128	3.0	2.3438	500	768
	M	⋯	192	2.0	1.5625	500	1536
	H	⋯	256	1.5	1.1719	500	2560
GRA48q1s0	L	⋯	128	3.0	2.3438	550	768
	M	⋯	192	2.0	1.5625	550	1536
	H	⋯	256	1.5	1.1719	550	2560
GRA50q1s0	L	⋯	128	3.0	2.3438	800	768
	M	⋯	192	2.0	1.5625	800	1536
	H	⋯	256	1.5	1.1719	800	2560

$$\langle h_1, h_2 \rangle = 4\Re \int \frac{\tilde{h}_1(f)\tilde{h}_2^*(f)}{S_n(f)} df. \tag{14}$$

Here the $\tilde{h}_1(f)$ and $\tilde{h}_2(f)$ are the Fourier transforms of the time domain waveforms. In this work we consider a uniform power spectral density (PSD) [$S_n(f) \equiv 1$] unless explicitly stated. In such case, we have noted that the power of the signals is localized in the frequency interval $Mf \in [0.005, 0.1]$ in geometric units, so that we compute the integrals in this range. We have checked that the power is concentrated in this interval for all of our simulations. In turn, the unfaithfulness, or mismatch, is given by $\bar{\mathcal{F}} = 1 - \mathcal{F}$. The unfaithfulness, which ranges in [0,1], is equal to the fractional loss of signal-to-noise ratio due to the difference between the two compared waveforms. We compute the matches using the algorithm `optimized_match` implemented in PyCBC, which efficiently aligns the waveforms optimizing over the differential phases and time shifts.

G. Consistency of the numerical results

We discuss the consistency of the results obtained with Einstein Toolkit and GR-Athena++, focusing on simulations ETK42q1s0, 48q1s0, 50q1s0. This will provide error estimates for our NR simulations needed to assess the EOB/NR comparisons later on.

We consider three resolutions, resulting from taking $\delta x = \{3, 4, 6\}M$ at the coarsest level for Einstein Toolkit and $N_M = \{256, 192, 128\}$ for GR-Athena++, since their corresponding puncture resolutions match. We summarize the relevant technical information for these simulations in Table II. In the main text, we focus on the amplitude and phase differences for the leading modes (2,2) of the strain, and comment on some other observables in the Appendixes.

1. Self-convergence

We begin by decomposing the leading modes in amplitude and phase as in (5). We compare these for different resolutions as a function of time, performing time interpolation of third order. Let us denote the amplitudes and phases at a given resolution by $A_{L,M,H}$, $\phi_{L,M,H}$. We can claim convergence of order r if

$$\frac{A_H - A_M}{A_L - A_M} \approx SF(r), \tag{15}$$

where the scaling factor SF is given by

$$SF(r) = \frac{\delta x_H^r - \delta x_M^r}{\delta x_M^r - \delta x_L^r}, \tag{16}$$

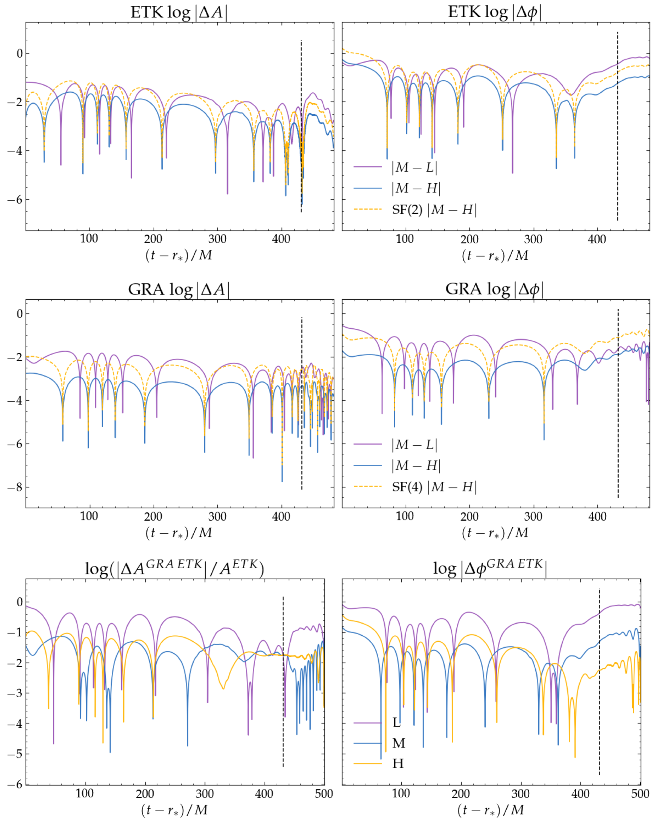

FIG. 3. Self-convergence for `ETK50q1s0` (top row) and for `GRA50q1s0` (middle row). Displayed are the differences in amplitude and phase for consecutive resolutions $(L-M)$, $(M-H)$. In addition, we overlay the curves for $SF(r)(M-H)$ which allows us to test for convergence of a given order r, see (16), which we show in each panel. Bottom row: comparison between `ETK50q1s0` and `GRA50q1s0` at fixed resolution. The simulations for (L, M, H) resolutions have the same grid spacing at puncture location, see Table II. For each case, we display the absolute value of the difference in normalized amplitude and phase for every available resolution.

and similarly for the phases, see e.g. [64]. Note that the left-hand side of (15) is a varying function of time, so that convergence can vary during different stages of the waveform. We show sample results for self-convergence as a function of time for simulations `ETK50q1s0` and `GRA50q1s0` in Fig. 3. Note that to ease the visualization of the relation (15) we do not normalize the amplitude differences. We record the (normalized) amplitude and phase differences at merger, along with the waveform mismatches in Table III.

Our data for `ETK50q1s0` is compatible with second-order convergence before merger, while near and after merger the convergence order increases to fourth order. The time-dependent self-convergence results are compatible with the behavior of the mismatches shown in Table III, which also decrease with increasing resolution. In the case of GR-Athena++, we observe convergence of order 4 or higher before merger, but after merger the convergence rate for the phase worsens. The mismatches also decrease with increasing resolution.

The self-convergence results for the (normalized) amplitude and phase differences at merger in Table III can be taken as a proxy for the accuracy of the NR simulations when comparing to EOB. Roughly speaking, differences between medium resolution simulations (used for the bulk of our simulations) and high resolution is around 0.1% for the amplitude and of the order of 0.01 radians for the phases.

2. *Code comparison*

We now focus on the comparison between Einstein Toolkit and GR-Athena++. We display the amplitude and phase differences as a function of time for the leading modes of `ETK50q1s0` and `GRA50q1s0` at the bottom of Fig. 3. The cases `ETK42q1s0, 48q1s0` and `GRA42q1s0, 48q1s0`

TABLE III. Self-convergence results for the $\ell = m = 2$ strain mode for consecutive resolutions for Einstein Toolkit and GR-Athena++ at merger time. From left to right, the columns report: the relative amplitude differences, the phase differences, and the unfaithfulness between two consecutive resolutions.

ID	$\mathrm{Res}_{1,2}$	$\Delta A_{22,\mathrm{mrg}}^{\mathrm{res}_1-\mathrm{res}_2}/A_{22,\mathrm{mrg}}^{\mathrm{res}_1}$	$\Delta\phi_{22,\mathrm{mrg}}^{\mathrm{res}_1-\mathrm{res}_2}$	$\bar{\mathcal{F}}$
`ETK42q1s0`	L,M	-1.86×10^{-3}	2.265×10^{-3}	7.469×10^{-6}
`ETK42q1s0`	M,H	-3.29×10^{-3}	-2.95×10^{-3}	1.101×10^{-4}
`ETK48q1s0`	L,M	-9.73×10^{-3}	-4.55×10^{-2}	2.048×10^{-4}
`ETK48q1s0`	MH	-3.47×10^{-3}	-2.02×10^{-2}	7.393×10^{-5}
`ETK50q1s0`	L,M	-1.02×10^{-3}	-3.63×10^{-1}	1.917×10^{-3}
`ETK50q1s0`	M,H	-1.33×10^{-5}	-5.85×10^{-2}	5.463×10^{-5}
`GRA42q1s0`	L,M	-1.32×10^{-3}	5.257×10^{-3}	9.756×10^{-6}
`GRA42q1s0`	M,H	-1.14×10^{-3}	1.715×10^{-3}	1.332×10^{-6}
`GRA48q1s0`	L,M	-2.74×10^{-3}	1.686×10^{-2}	1.352×10^{-5}
`GRA48q1s0`	M,H	-2.65×10^{-4}	-8.38×10^{-3}	9.574×10^{-6}
`GRA50q1s0`	L,M	-6.56×10^{-3}	2.204×10^{-2}	9.405×10^{-5}
`GRA50q1s0`	M,H	-1.06×10^{-3}	-1.30×10^{-2}	1.484×10^{-5}

TABLE IV. Comparing the $\ell = m = 2$ strain waveform at merger obtained with Einstein Toolkit and GR-Athena++. From left to right, the columns report: the relative amplitude differences, the phase differences at merger and the unfaithfulness for the three configurations simulated with both codes at (L, M, H) resolution.

ID	Res	$\Delta A^{\rm GRAETK}_{22,\rm mrg}/A^{\rm GRA}_{22,\rm mrg}$	$\Delta\phi^{\rm GRAETK}_{22,\rm mrg}$	$\bar{\mathcal{F}}$
42q1s0	L	1.640×10^{-2}	1.731×10^{-2}	5.417×10^{-5}
	M	1.567×10^{-2}	1.364×10^{-2}	1.788×10^{-5}
	H	1.355×10^{-2}	9.073×10^{-3}	9.145×10^{-5}
48q1s0	L	2.427×10^{-2}	8.193×10^{-2}	2.216×10^{-4}
	M	1.704×10^{-2}	1.973×10^{-2}	1.991×10^{-5}
	H	1.388×10^{-2}	7.851×10^{-3}	1.538×10^{-5}
50q1s0	L	1.099×10^{-2}	4.363×10^{-1}	2.117×10^{-3}
	M	1.737×10^{-2}	5.084×10^{-2}	2.721×10^{-5}
	H	1.848×10^{-2}	5.683×10^{-3}	2.206×10^{-6}

behave similarly. We summarize the information regarding the differences at merger and mismatches in Table IV. For the three simulations, we find that the waveforms are most coincident at medium resolution. In this case, the amplitude difference at merger is of order 2%, being always higher for GR-Athena++. This is compatible with the results of [54] which found a 2% difference at merger with the BAM code [65]. While we observe some decrease of the amplitude difference at merger values for high resolution, it is not clear whether they will converge away with increasing resolution further. On the other hand, the phases at merger appear to be converging with increasing resolution, the differences ranging from 10^{-2} to 10^{-3}. At medium resolution, which is the one used for Einstein Toolkit in the bulk of this work, we find that the differences with GR-Athena++ are roughly of the order of 1% for the amplitude and 0.01 radians for the phase.

The mismatches for Einstein Toolkit and GR-Athena++ leading modes at medium resolution are of order 10^{-5}, and show convergent behavior for `ETK48q1s0, 50q1s0` (`GRA48q1s0, 50q1s0`) but not for `ETK42q1s0` (`GRA42q1s0`).

We emphasize that the comparisons discussed above involve the leading modes of the extrapolated strain. However, we should keep in mind that the NR results are also affected by our choice of time integration and extrapolation to infinity. We provide a comparison of the raw data by considering the unextrapolated ψ_4 scalars produced by Einstein Toolkit and GR-Athena++ in Appendix B 1.

III. EFFECTIVE-ONE-BODY MODEL

In this work we will use the eccentric version of the `TEOBResumS` [34,66] effective-one-body (EOB)-based [67,68] waveform model, dubbed `TEOBResumS-Dalì`, as defined in Refs. [36,69]. The promotion of the quasicircular model to the eccentric case follows the idea of Ref. [35] of incorporating noncircular effects in the Newtonian prefactors in both the waveform and radiation reaction.[1] We refer the reader to Ref. [36] and references therein for most of the technical details of the model. Here it is only worth recalling that the EOB description of the merger and ringdown is based on suitable fits of *quasicircular* ringdown waveforms [28,34]. This approximation looks sufficiently accurate for bound configurations, because the eccentric inspiral has the time to progressively circularize towards merger [36]. By contrast, for dynamical capture configurations this is not the case and the quasicircular ringdown can be inaccurate [7,45]. For this reason, one of the final goals of this paper is to show how to use our new NR simulations to suitably improve the model during merger and ringdown. Before discussing this, let us recall that any EOB model essentially depends on two sets of parameters that are informed by NR simulations: (i) on the one hand, there are those that directly appear in the dynamics, i.e. as effective modifications to the EOB Hamiltonian. Belonging to this class are the effective 5PN parameter a_6^c entering the A potential of `TEOBResumS` or the effective next-to-next-to-next-to-leading order parameter c_3 used to improve the corresponding spin-orbit coupling; and (ii) on the other hand, there are parameters used to improve the shape of the waveform during plunge up to merger via the next-to-quasicircular (NQC) correction or to accurately describe the postmerger-ringdown signal. In this paper we do not focus on exploring the effect of the dynamical parameters, the values of which we set to those determined in [36], but rather explore the impact of informing the remaining ones using data from our dynamical capture BBH simulations. In particular, we want to: (i) obtain new, NR-informed, next-to-quasicircular corrections to the waveform and (ii) use a new NR-informed merger and ringdown model.

[1] Higher order noncircular PN corrections have been computed in Refs. [70–72], but they have not been implemented yet in the version of `TEOBResumS-Dalì` employed in this work.

Since our NR simulations cover parameter space in a sparse way, we can only use the NR information separately for each dataset, and cannot present global fits of the NR-informed parameters designed to cover the full parameter space. We therefore aim to illustrate what is needed to improve the current model for hyperbolic capture and quantify the improvement, leaving the development of global fits for future work. From now on, we will focus only on the quadrupole waveform for simplicity, although the same approach could be extended to the other multipoles. We decompose it in amplitude and phase as

$$h_{22} = A_{22} e^{-i\phi_{22}}, \tag{17}$$

where both (A_{22}, ϕ_{22}) are functions of time t. The waveform frequency is $\omega_{22} \equiv \dot{\phi}_{22}$. In addition, we will use the ν-normalized waveform amplitude $\hat{A}_{22} \equiv A_{22}/\nu$. Following the standard TEOBResumS procedure for quasicircular binaries [34,66], we count four parameters related to NQC corrections and seven parameters needed to model the postmerger-ringdown part of the waveform. In practice, one needs to extract *11* numbers from each NR simulation. The NR-informed parameters are

(i) The four NQC parameters $(a_1^{22}, a_2^{22}, b_1^{22}, b_2^{22})$ that enter the NQC waveform correction

$$\hat{h}_{22}^{\rm NQC} = (1 + a_1^{22} n_1^{22} + a_2^{22} n_2^{22}) e^{\mathrm{i}(b_1 n_3^{22} + b_2 n_4^{22})}. \tag{18}$$

Here, the functions n_i^{22} define the NQC basis [see in particular text around Eq. (13) of Ref. [36]], and are determined by imposing continuity between the EOB waveform and the NR amplitude and frequency values $(\hat{A}^{\rm NR}_{\rm NQC}, \dot{\hat{A}}^{\rm NR}_{\rm NQC}, \omega^{\rm NR}_{\rm NQC}, \dot{\omega}^{\rm NR}_{\rm NQC})$ evaluated at the NQC extraction time $t^{\rm NR}_{\rm NQC}$. For each mode, $t^{\rm NR}_{\rm NQC} = t^{\rm NR}_{A^{\max}} + 2M$, where $t^{\rm NR}_{A^{\max}}$ is the location of the amplitude's peak.

(ii) The five parameters entering the ringdown template as introduced in Ref. [28]:

$$\theta^{\rm RD} = (\hat{A}_{\max}, \omega_{\max}, c_3^A, c_\phi^3, c_\phi^4). \tag{19}$$

The values of the amplitude and frequency at amplitude maximum $(A_{\max}, \omega_{\max})$ are directly read from the NR waveform. By contrast, the parameters $(c_3^A, c_\phi^3, c_\phi^4)$ are obtained by fitting the postmerger-ringdown waveform following [28].

(iii) The postmerger template also depends on the (complex) frequency of the first two quasinormal modes that are determined from the mass and dimensionless spin of the final black hole $(M_f, \hat{a}_f)$ interpolating the tables of Ref. [73].

Table V lists all the NR-informed parameters for each NR dataset considered. The last two columns also report the EOB/NR difference in the binding energy at merger and the phase difference $\Delta\phi_{22}^{\rm EOBNR} \equiv \phi_{22}^{\rm EOB} - \phi_{22}^{\rm NR}$. Note that the latter is computed, as we will see below, using an *improved* model with the NR-informed ringdown for each dataset. The origin of these numbers will be discussed in detail in Sec. IV below.

A. Connecting NR initial data with EOB ones

In order to compare our results from NR and EOB, we need to specify which parameters we shall input in TEOBResumS based on the initial NR data. Initial data for dynamical capture in TEOBResumS are given by fixing the mass ratio q, initial energy $E_{\rm EOB}/M$, dimensionless initial orbital angular momentum $p_\varphi = L^{\rm EOB}/(\mu M)$, dimensionless spins $\chi_{1,2}^{\rm EOB} \equiv S_i/m_i^2$ and initial separation $r_{\rm EOB}$. In practice, the initial EOB parameters are obtained by identifying the NR and EOB spin values, i.e. $\chi_{1,2}^{\rm EOB} = \chi_{1,2}^{\rm NR}$, and matching the other dynamical quantities to the initial ADM values from NR simulations as

$$E_{\rm EOB} = E_0^{\rm ADM} + \Delta E_{\rm EOB}, \tag{20}$$

$$L_{\rm EOB} = J_0^{\rm ADM} - (S_1 + S_2) + \Delta J_{\rm EOB}, \tag{21}$$

$$r_{\rm EOB} = D + \Delta r_{\rm EOB}, \tag{22}$$

where $(\Delta E_{\rm EOB}, \Delta J_{\rm EOB}, \Delta r_{\rm EOB})$ are arbitrary corrections to the NR quantities to be determined as follows. We choose the initial EOB distance $\Delta r_{\rm EOB}$ such that the EOB waveforms extend to earlier times at least as much as the NR simulations. For this reason, we choose $\Delta r_{\rm EOB} = 4M$. Following [7], values of $(\Delta E_{\rm EOB}, \Delta J_{\rm EOB})$ are chosen by minimizing the EOB/NR mismatch. More precisely, when performing this minimization we consider both the ringdown and NQC information in the EOB waveform. We implement this using the algorithm dual_annealing from the SciPy Python library [74]. We find that we obtain a good match for the signal length considering $|\Delta E_{\rm EOB}| < 0.0007 E_{\rm ADM}$, $|\Delta J_{\rm EOB}| < 0.006 J_{\rm ADM}$, see Table I.

Although this method is efficient and successful, we have to remind the reader that at a rigorous mathematical level the initial puncture parameters expressed in ADM coordinates (relative separation and momenta) should be connected to the corresponding EOB ones by using the corresponding canonical transformation. This was originally obtained in Ref. [67] at 2PN accuracy. One of the uses of this transformation, already suggested in Ref. [67], was to provide small-eccentricity initial data for NR simulations. This idea was eventually implemented in Ref. [75] at 3PN accuracy. For completeness, here we also explored this route by converting the ADM quantities $(\vec{P}^{\rm ADM}, D)$ to EOB ones $(E_{\rm EOB}, p_\varphi^{\rm EOB}, r_{\rm EOB})$ using the canonical transformation at 2PN. Figure 4 focuses on two datasets, ETK48q1s0

TABLE V. Informing the EOB model with NR data. From left to right the columns report: the name of the dataset, the ν-normalized quadrupole waveform amplitude at merger time $\hat{A}_{22}^{\max} = A_{22}^{\max}/\nu$ and the corresponding frequency; the mass M_f and dimensionless angular momentum $\hat{a}_f \equiv J_f/M_f^2$ of the final remnant black hole; the NR values used to determine the NQC corrections; the NR-informed parameters of the postmerger fit. The last two columns report the EOBNR difference in the binding energy per reduced mass at merger $\delta E_{b,\mathrm{mrg}}^{\mathrm{EOBNR}} \equiv E_{b,\mathrm{mrg}}^{\mathrm{EOB}} - E_{b,\mathrm{mrg}}^{\mathrm{NR}}$ and the corresponding phase difference at merger obtained using the NR-informed upgraded model.

No.	ID	$\hat{A}_{22}^{\max}$	$\omega_{22}^{\max}$	M_f	a_f	$\hat{A}_{\mathrm{NR}}^{\mathrm{NQC}}$	$\dot{\hat{A}}_{\mathrm{NR}}^{\mathrm{NQC}}$	$\omega_{\mathrm{NR}}^{\mathrm{NQC}}$	$\dot{\omega}_{\mathrm{NR}}^{\mathrm{NQC}}$	c_3^A	c_3^ϕ	c_4^ϕ	$\tilde{\delta}E_{b,\mathrm{mrg}}$	$\Delta\phi_{22,\mathrm{mrg}}^{\mathrm{EOBNR}}$ [rad]
1	`ETK37q1s0`	1.419	0.335	0.978	0.685	1.399	−0.020	0.369	0.017	−0.016	1.74076	0.39046	+0.0045	−0.003
2	`ETK42q1s0`	1.675	0.370	0.965	0.725	1.659	−0.016	0.398	0.014	−0.187	2.48789	0.73609	+0.0038	−0.008
3	`ETK44q1s0`	1.768	0.388	0.958	0.728	1.754	−0.015	0.410	0.011	−0.243	3.24197	1.19834	+0.0039	−0.029
4	`ETK46q1s0`	1.821	0.377	0.949	0.716	1.814	−0.007	0.394	0.009	−0.510	5.30479	1.33265	+0.0025	−0.015
5	`ETK48q1s0`	1.518	0.346	0.950	0.675	1.509	−0.010	0.370	0.012	−0.422	4.42020	1.91359	+0.0030	−0.096
6	`ETK50q1s0`	1.679	0.364	0.949	0.697	1.671	−0.008	0.383	0.010	−0.477	4.80545	1.26372	+0.0033	−0.011
7	`ETK42q1s050-`	1.429	0.307	0.981	0.515	1.409	−0.020	0.336	0.014	0.001	1.59410	0.28785	+0.0041	−0.030
8	`ETK42q1s025-`	1.522	0.338	0.976	0.626	1.506	−0.017	0.367	0.014	−0.072	2.07120	0.53770	+0.0040	−0.012
9	`ETK42q1s025++`	1.863	0.403	0.943	0.793	1.849	−0.015	0.425	0.012	−0.459	5.39366	2.68358	+0.0025	−0.035
10	`ETK42q1s050++`	1.487	0.428	0.940	0.832	1.476	−0.012	0.453	0.013	−0.093	2.87101	1.14302	+0.0057	0.014
11	`ETK42q1s050+-`	1.676	0.370	0.965	0.724	1.660	−0.017	0.398	0.014	−0.181	2.49269	0.73682	+0.0038	−0.012
12	`ETK42q1.5s0`	1.763	0.374	0.962	0.707	1.748	−0.015	0.398	0.012	−0.297	3.17798	1.12475	+0.0029	−0.003
13	`ETK42q2s0`	1.734	0.327	0.957	0.633	1.730	−0.004	0.338	0.006	−0.845	9.62619	1.39233	−0.0003	−0.026
14	`ETK42q2.15s0`	1.681	0.337	0.963	0.630	1.674	−0.007	0.358	0.011	−0.597	−0.00004	0.00001	+0.0030	+0.032

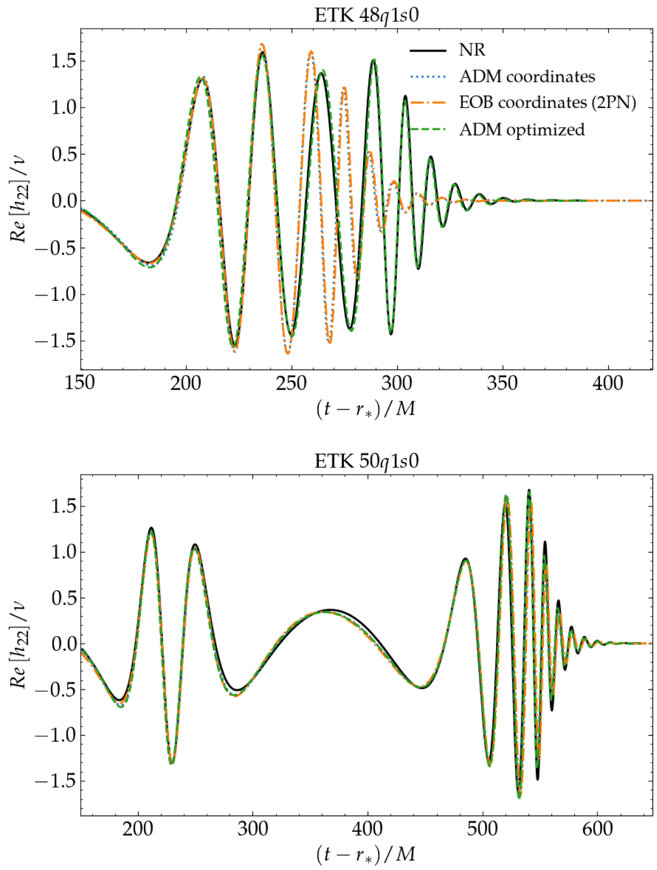

FIG. 4. Relation between NR initial data and EOB ones for two selected configurations. The procedure of tuning phenomenological corrections to $(E_0^{\rm ADM}, J_0^{\rm ADM})$ using Eqs. (20) and (21) is globally more efficient (especially for the ETK48q1s0 dataset) than the straightforward transformation from ADM to EOB coordinates.

and ETK50q1s0: the NR waveforms (black) are compared with EOB waveforms obtained with different choices of initial conditions. We note that the impact of the optimization and of the canonical transformation (that typically is rather small) depend on the configuration. For ETK48q1s0 the effect of the ADM/EOB canonical transformation is practically negligible, while the phenomenological optimization is more efficient in obtaining the correct initial data. By contrast, for ETK50q1s0 the various choices are practically equivalent.

IV. EOB/NR COMPARISONS

Let us finally focus on the bulk of our results about direct comparisons between EOB and NR waveforms. As usual, we provide two different metrics: (i) phase and amplitude differences in the time domain; and (ii) EOB/NR unfaithfulness as defined from Eq. (13) above. In addition, we will also discuss comparisons between the EOB and NR dynamics, as expressed using the gauge-invariant relation between energy and angular momentum.

A. Time-domain phasing and unfaithfulness

The EOB/NR amplitude and phase differences are defined

$$\Delta A_{22}^{\rm EOBNR} \equiv A_{22}^{\rm EOB} - A_{22}^{\rm NR}, \tag{23}$$

$$\Delta \phi^{\rm EOBNR} \equiv \phi_{22}^{\rm EOB} - \phi_{22}^{\rm NR}, \tag{24}$$

and are computed once the two waveforms are aligned after fixing an arbitrary time and phase shifts (τ, α). This is done by minimizing the unfaithfulness (in zero noise) as defined from Eq. (13) above, computed using the algorithm `optimized_match` of the PyCBC library [76].

1. Nonspinning configurations

Let us discuss first nonspinning configurations, i.e. datasets from ETK31q1s0 to ETK50q1s0 (equal mass) and ETK42q1.5s0 to ETK42q2.15s0 (unequal mass). Focusing first on equal-mass case binaries, the phenomenology changes from a direct capture, ETK31q1s0, to a double encounter, ETK50q1s0. The corresponding EOB/NR time-domain phasing comparisons are shown in Fig. 5. The top panels show the real part of the waveform and the instantaneous gravitational wave frequency, as obtained using the full NQC and ringdown improved model. The bottom panels exhibit the phase difference and the relative amplitude differences obtained with four different versions of the waveform: (i) the standard, TEOBResumSDalì one with the native ringdown informed by quasicircular information; (ii) the model with NR-informed NQC corrections; (iii) the model with NR-informed NQC corrections and NR-informed merger values of $(\hat{A}_{\rm max}, \omega_{\rm max})$; and (iv) the full improved model corresponding at the top panel, completed by the NR-informed complete postmerger waveform. The phase differences at merger corresponding to case (iv) above are listed in Table V. The bottom panels of Fig. 5 indicate that the NR information injected in the merger-ringdown description may bring a reduction of the order of ~0.1 rad of the phase difference during the final phases of the coalescence. The differences during either the precursor (for ETK31q1s0) or the first encounter (for ETK50q1s0) are of the order of 0.1 rad, with trends that suggest that some additional analytic improvement, either in the dynamics or in the waveform [72], might be needed to reach the NR accuracy level. Despite this, the corresponding values of the EOB/NR unfaithfulness $\bar{F}$ are more than acceptable, as we will see below. Before presenting this calculation, let us focus on the few, nonspinning, dataset with $q \neq 1$. The purpose of this choice was to reliably extract from NR also higher waveform modes and use them to test the corresponding EOB multipoles, tested so far only for eccentric inspirals [36]. This is done in Fig. 6, which shows the complete

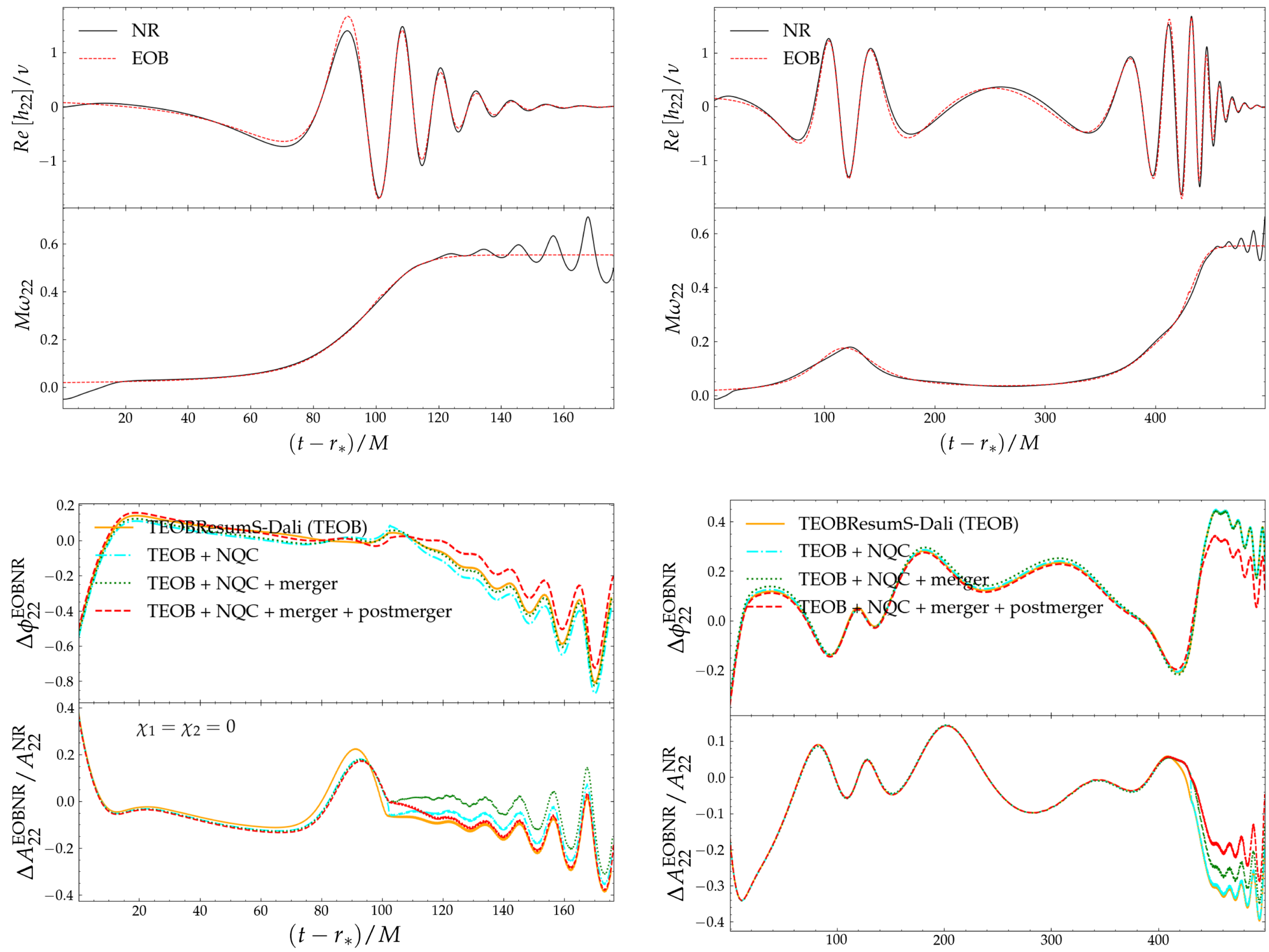

FIG. 5. Equal-mass, nonspinning case. EOB/NR waveform comparison. Top panels: $\ell = m = 2$ real part and frequency evolution for `ETK42q1s0` (left) and `ETK50q1s0` (right). Bottom panels: EOB/NR phase and (relative) amplitude differences obtained by increasing progressively the amount of NR input to describe the merger and ringdown part.

EOB/NR comparison for modes $\{(2,2),(2,1),(3,3),(3,2),(4,4),(5,5)\}$ for the dataset `ETK42q2.15s0` with $q = 2.15$. For this specific comparison we are using the standard `TEOBResumSDalì` model without NR information *also* in the (2,2) mode. Visually, the EOB/NR agreement is acceptable and can be evidently improved further by injecting NR information. Figure 6 also highlights inaccuracies in the recovering of the strain from ψ_4 from higher modes, as it is evident from the trend of the postmerger waveform for modes (4,4) and (5,5). We evaluate the impact of including the uninformed higher modes in the EOB/NR full strain in Appendix C. We find that the unfaithfulness remains below 0.01 for most simulations, with the exception of `ETK37q1s0`, pointing towards the significance of higher modes for the small angular momentum configurations.

The time-domain phasing analysis is complemented by the calculation of the unfaithfulness $\bar{\mathcal{F}}$. This is done either assuming zero noise, $S_n(f) = 1$, or using the zero-detuned, high power spectral density (PSD) design sensitivity of Advanced LIGO [77]. As it is standard for quasicircular binaries, this yields $\bar{\mathcal{F}}$ as function of the total mass. Assuming $S_n(f) = 1$, we explore how the increase of NR information used to correctly shape the merger-ringdown part of the waveform reflects on $\bar{F}$. The result of this analysis is found in Fig. 7. The values corresponding to the complete model are also listed in the last column of Table I. Note that the mismatches are highest for the smallest angular momenta simulation (corresponding to lowest scattering angle `ETK37q1s0` and antialigned spins `ETK42q1s050+-`, a dataset to be discussed below). In all other cases, the mismatches are below 1%, always obtained after the NR-information procedure. The calculation using the Advanced LIGO PSD is exhibited in Fig. 8 for total mass $20M_\odot \leq M \leq 200M_\odot$. It is remarkable to note that, despite the absence of any additional tuning on the actual dynamics of the binary (that was informed using only quasicircular simulations), one has $\bar{\mathcal{F}}^{\rm max} \sim 1\%$ all over the considered configurations.

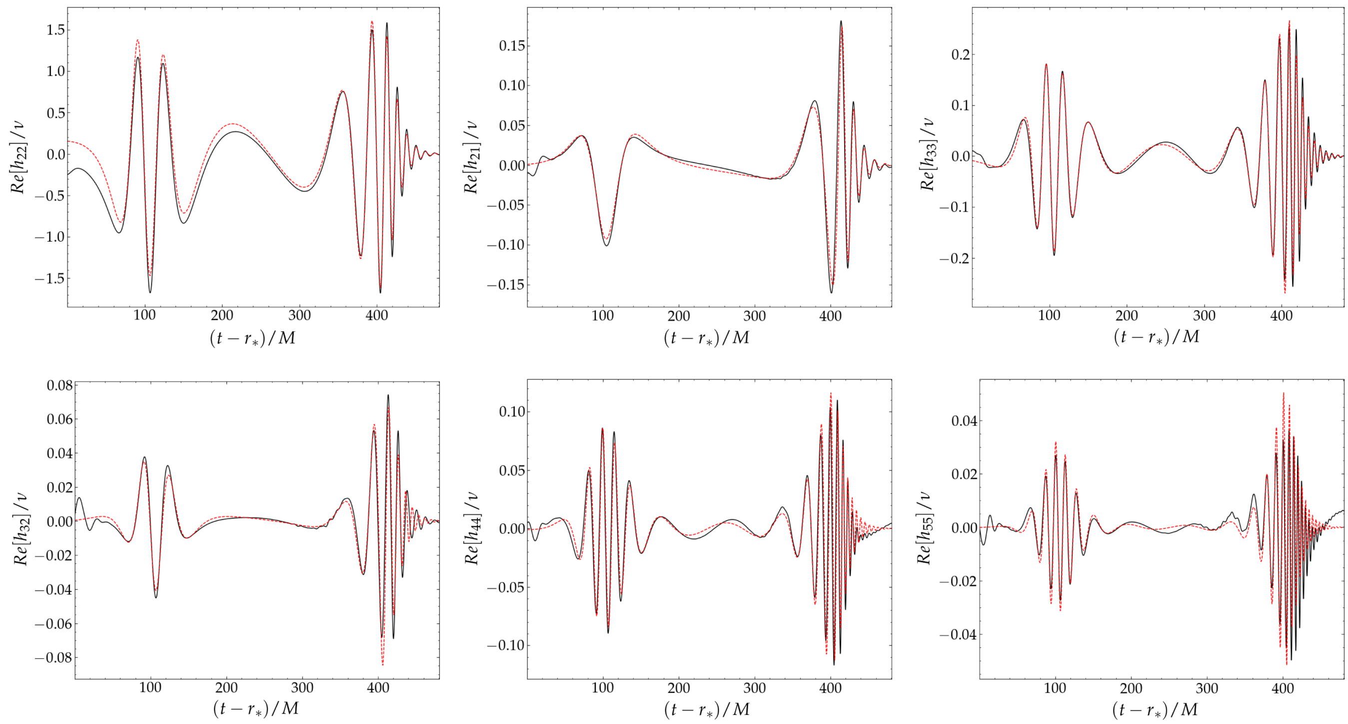

FIG. 6. Unequal-mass ($q = 2.15$), nonspinning case, dataset `ETK42q215`: EOB/NR phasing comparison including the available higher harmonics. Note that the (2, 2) mode is completed by the NR-informed, noncircular, merger, and ringdown, while the higher harmonics still retain the standard quasicircular contributions. Despite this, the agreement is acceptable. Also note some unphysical features in the ringdown for (4, 4) and (5, 5) due to the calculation of the strain from ψ_4.

2. Spin

We also considered a few datasets with spin aligned (or antialigned) with the orbital angular momentum. Before discussing their properties and putting them in relation with the EOB model, let us recall a pure EOB prediction presented in Ref. [16]. The effect of the BH spins (aligned or antialigned with the orbital angular momentum) for dynamical capture BBHs was analyzed in Sec. III A of Ref. [16]. The spin-orbit interaction implemented within the EOB model allowed for a very precise prediction for a $q = 1$ dynamical encounter of the changes in the waveform phenomenology with respect to the corresponding nonspinnig case. More precisely: (i) if spins are both aligned with angular momentum, the *repulsive* character of the interaction is such that a configuration that merges in the absence of spins can just scatter; (ii) if spins are both antialigned with the angular momentum, the *attractive*

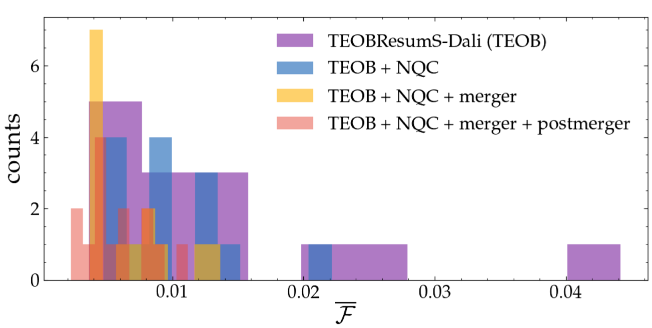

FIG. 7. EOB/NR unfaithfulness for the $\ell = m = 2$ mode obtained in zero noise for all configurations considered. Note how $\bar{\mathcal{F}}$ decreases due to the NR improvement of the merger and ringdown part of the EOB waveform.

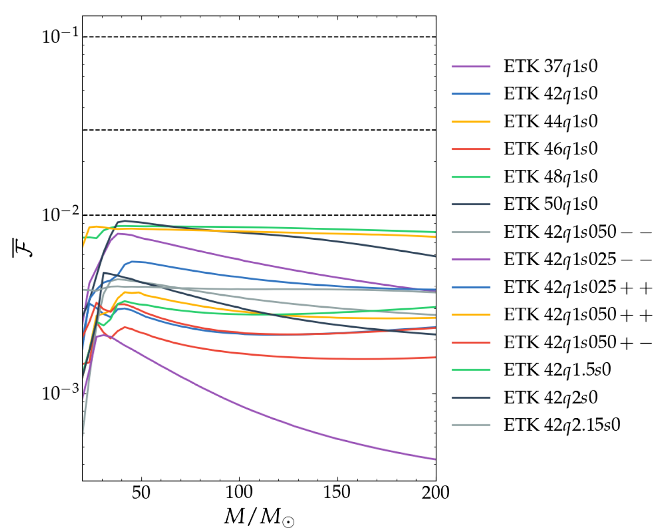

FIG. 8. EOB/NR unfaithfulness for the $\ell = m = 2$ mode obtained with the zero-detuned, high-power noise spectral density of Advanced LIGO [77].

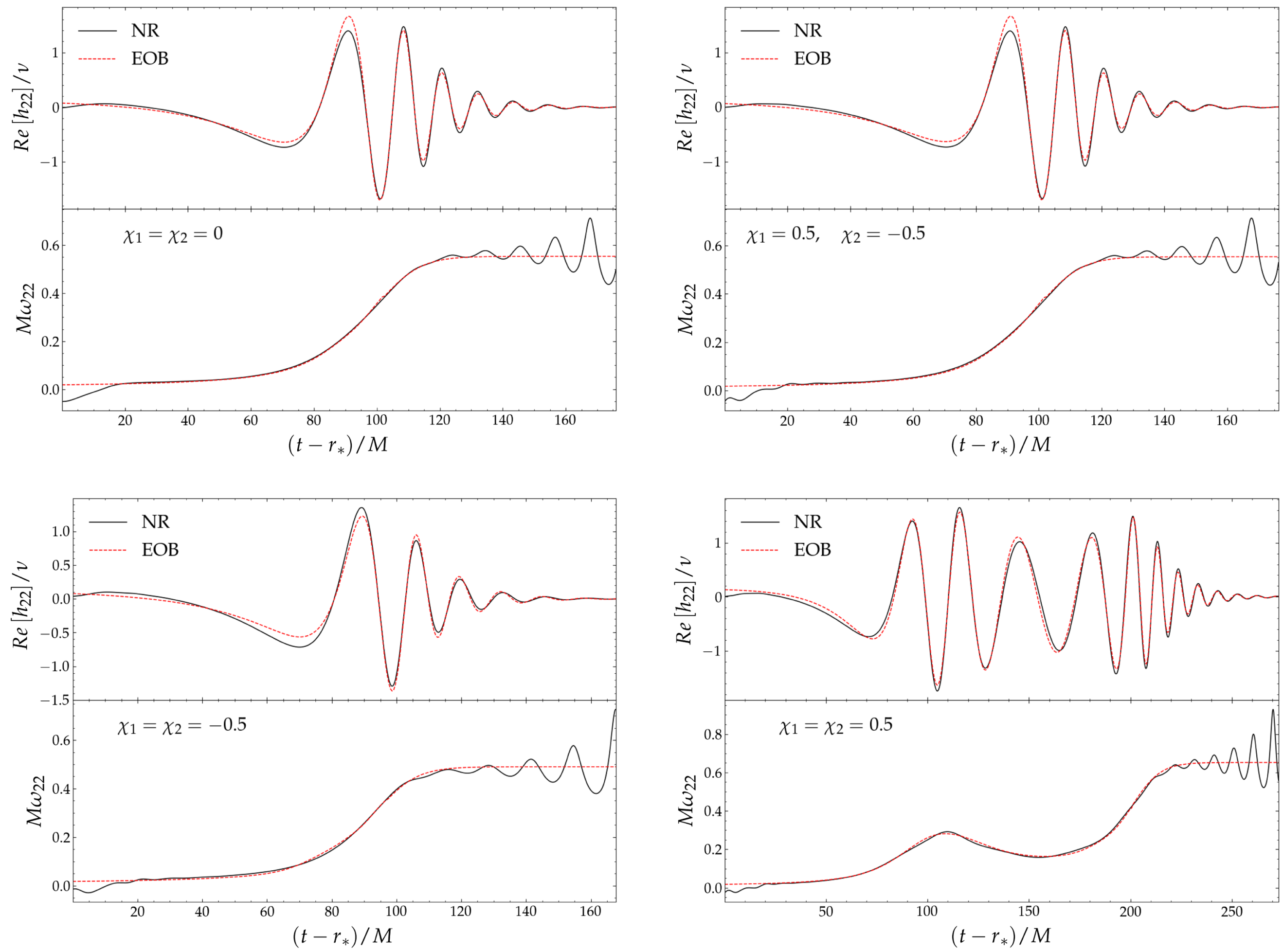

FIG. 9. EOB/NR comparisons for spin-aligned binaries. Top row: ETK42q1s* configurations with $\chi_1 = \chi_2 = 0$ (left) and $\chi_1 = -\chi_2 = 0.5$ (right). The cancellation of the spin-orbit interaction as predicted by the EOB model is present also in the NR data. Bottom panels: $\chi_1 = \chi_2 = -0.5$ (left) and $\chi_1 = \chi_2 = +0.5$ (right). When spins are negative, the plunge occurs faster and the signal is shorter than the $\chi_1 = \chi_2 = 0$ case. When spins are positive, the repulsive character of the spin-orbit coupling yields a first encounter followed then by the plunge and merger. The phase differences are reported in Fig. 10.

character of the spin-orbit interaction entails the plunge to occur on a shorter time scale; and (iii) if spins are one aligned and one antialigned with the orbital angular momentum the spin-orbit interaction cancels out and the corresponding waveform is substantially equivalent to the nonspinning one. This phenomenology is summarized in Fig. 6 of Ref. [16]. Here, we start from the nonspinning configuration ETK42q1s0 and add spins, with dimensionless magnitude $|\chi| = 0.25$ and $|\chi| = 0.5$ and different orientations. In this second case, we consider the three possible configurations, $\chi_1 = \chi_2 = +0.5$, $\chi_1 = \chi_2 = -0.5$ ad $\chi_1 = -\chi_2 = +0.5$ so to test the analytical prediction of Ref. [16] discussed above. Also here, as it was the case before, it is intended that the EOB waveform for each configuration is completed by the NR-informed NQC corrections and ringdown.

The first row of Fig. 9 displays the nonspinning simulation (left panel) and the one with misaligned spins (right panel). Both NR datasets are also compared with the corresponding EOB waveform (completed by the NR-informed description of merger and ringdown). We see that the analytical prediction of Ref. [16] is fully confirmed, with just very small differences between the waveforms due to spin-spin effects. The bottom row of the picture shows the case with both spins negative (left panel) and positive (right panel). In this second case, we see how the repulsive character of the spin-orbit interaction yields a first encounter (highlighted by the presence of a local maximum in the gravitational wave frequency) then followed by the merger. The actual EOB/NR phase differences are quantified in Fig. 10, which depicts together $\Delta\phi_{22}^{\rm EOBNR}$ for the four datasets.

B. Dynamics

We also compared the EOB and NR dynamics expressed using the gauge-invariant relation between energy and

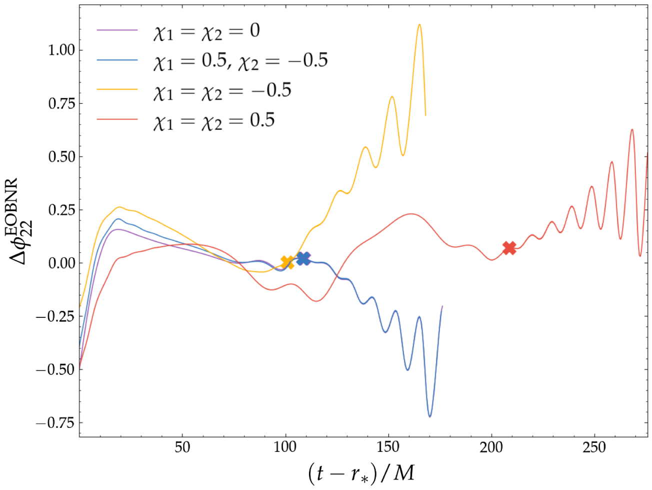

FIG. 10. EOB/NR phase differences for the configurations of Fig. 9. The markers indicate the location of the waveform amplitude peak. Note the rather small differences (only during the precursor phase) between the $\chi_1 = \chi_2 = 0$ and $\chi_1 = -\chi_2 = 0.5$ datasets.

angular momentum [60,61]. On the NR side, this quantity can be extracted as the parametric curves $(j(t), E_b(t))$ given by Eq. (11) for $t > t_{\rm junk}$. On the EOB side, this is just obtained from the evolution of the Hamiltonian dynamics. Note in this respect that it is *not* computed from the waveform multipoles as in the NR case. We gather the plots for all simulations in Appendix E, and list in Table V as meaningful values only the differences at merger. It is interesting to note that EOB/NR differences decrease monotonically with all physical parameters J_i, q, and χ, i.e. as the signals become longer and thus closer to the quasicircular simulations used to inform the model.

V. CONCLUSIONS

We have presented new NR simulations of black hole binaries, which can be interpreted as the late stages of dynamical captures. Our set of simulations includes some of the configurations of Gold and Brügmann [23] (see also [17]), improving the systematic exploration of aligned spins and mass ratio effects. The runs were mostly done using the Einstein Toolkit NR code. A few configurations were also simulated using the GR-Athena++ code for mutual cross-checking. The NR strain waveforms (computed here for the first time) are first compared with the state-of-the-art eccentric model TEOBResumS and additionally used to inform it to obtain improved accuracy for merger and ringdown. Our results on the NR side can be summarized as follows:

(i) We have systematically analyzed configurations with spins. We found that the analytical EOB predictions due to spin-orbit interaction of Ref. [16] in spin-aligned encounters (see Fig. 9) are fully confirmed by NR simulations. More precisely, if the spins are positive, the system has more GW cycles before merger than in the nonspinning case (repulsive character of spin-orbit interaction); if the spins are both negative, the plunge occurs faster with less cycles (attractive character of spin-orbit interaction); when the spins are misaligned and equal (one positive and one negative), the dynamics and waveforms are fully compatible with the nonspinning case.

(ii) We presented the first direct comparisons between Einstein Toolkit and GR-Athena++, corresponding to three different nonspinning equal-mass dynamical captures, previously studied in Ref. [23]. The comparison between the codes shows good quantitative agreement (Sec. II G 2), and the independent codes display self-convergence (Sec. II G 1).

(iii) We have systematically computed the strain waveform (that was absent in Ref. [23]) for both Einstein Toolkit and GR-Athena++, increasing the amount of currently known information (see in particular the supplemental material of Ref. [7], where three more configurations obtained with GR-Athena++ were presented). The computation of the strain from ψ_4 is one of the main technical challenging aspects of these simulations, and gets worse for higher modes. These difficulties point to the need of directly extracting the strain at infinity from NR simulations using well-known techniques based on Regge-Wheeler-Zerilli perturbation theory [78–81] or even using Cauchy characteristic extraction [82–84]. See also [85] for an alternative way of performing parameter inference that uses ψ_4 directly.

(iv) We computed, for the first time, the relation between energy and angular momentum, extending work previously done only for quasicircular binaries [60,61,86].

On the EOB side, our results can be summarized as follows:

(i) To start with, we compare the 14$\ell = m = 2$ NR waveforms obtained with the waveforms obtained using the state-of-the-art EOB model TEOBResumS-Dalì. The computation of the EOB/NR mismatch in white noise is ~1.5% for all datasets except for those configurations with the lowest angular momentum, that reach ~4%. This is by itself a remarkable result considering that TEOBResumS-Dalì was only informed by quasicircular NR simulations [36].

(ii) We report good agreement also for higher modes. Notably, for double encounter configurations, this is true also for the first burst of radiation. This suggests that the accuracy of the multipolar Newtonian prefactor in the waveform, introduced in Ref. [35], and only tested for bound configurations [36], is maintained also for hyperbolic encounters.

(iii) We then used NR simulations to improve the EOB model, notably the $\ell = m = 2$ merger and ringdown part. We found that the accuracy of the EOB ringdown is mostly dominated by the values of amplitude and frequency at merger and of the mass and spin of the final black hole. When these values are incorporated in the model, as well as NR-informed NQC corrections, the EOB/NR mismatches are at most 1.1% for all the simulations considered.

Our analysis lays out the procedure of informing TEOBResumS-Dalì incorporating NR data, showcasing that the model is sufficiently accurate for future searches of dynamical encounters signals. Future work will focus on a systematic numerical investigation of dynamical encounters and present global fits of the merger and ringdown parameters to inform TEOBResumS-Dalì. We thus expect to obtain a highly faithful extension of TEOBResumS-Dalì for parameter estimation of dynamical capture and highly eccentric events, which will allow for further reassessment of the events observed by LVK so far.

ACKNOWLEDGMENTS

We thank Juan García-Bellido and Santiago Jaraba for insightful discussions on NR simulations of hyperbolic encounters and related matters, and Mark Gieles for valuable comments on rates of eccentric mergers. We thank all the participants of the "Workshop on Gravitational Wave Modelling" held in Barcelona (2022) and of the "EOB@Work 2023" workshop in Jena. The work of T. A. is supported in part by the ERC Advanced Grant No. GravBHs-692951, by the Ministry of Science and Innovation (EUR2020-112157, PID2021-125485NB-C22, CEX2019-000918-M funded by MCIN/AEI/10.13039/501100011033), and by AGAUR (SGR-2021-01069). R. G. acknowledges support from the Deutsche Forschungsgemeinschaft (DFG) under Grant No. 406116891 within the Research Training Group RTG 2522/1. S. B. acknowledges support from the EU H2020 under ERC Starting Grant No. BinGraSp-714626, from the EU Horizon under ERC Consolidator Grant, No. InspiReM-101043372. J. C. B. is supported by a fellowship from "la Caixa" Foundation (ID 100010434) and from the European Union's Horizon 2020 research and innovation program under the Marie Sklodowska-Curie Grant Agreement No. 847648. The fellowship code is LCF/BQ/PI20/11760016. J. C. B. is also supported by the Research Grant No. PID2020–118635GB-I00 from the Spain-Ministerio de Ciencia e Innovación. N. S. G. is supported by the Spanish Ministerio de Universidades, through a María Zambrano grant (Grant No. ZA21-031) with Reference No. UP2021-044, within the European Union-Next Generation EU. J. A. F. is supported by the Spanish Agencia Estatal de Investigación (Grants No. PGC2018-095984-B-I00 and No. PID2021-125485NB-C21) funded by MCIN/AEI/10.13039/501100011033 and ERDF A way of making Europe, by the Generalitat Valenciana (Grant No. PROMETEO/2019/071), and by the European Union's Horizon 2020 research and innovation (RISE) program H2020-MSCA-RISE-2017 Grant No. FunFiCO-777740. The work of D. R. was supported by NASA under Award No. 80NSSC21K1720. We are grateful to P. Micca for, never trivial, inspiring suggestions. TEOBResumS is publicly available [87]. The Einstein Toolkit simulations were performed at Lluis Vives cluster for scientific calculations at University of Valencia [88] and MareNostrum4 at the Barcelona Supercomputing Center (Grants No. AECT-2022-3-0001 and No. AECT-2022-2-0006). The GR-Athena++ simulations were performed on the national HPE Apollo Hawk at the High Performance Computing Center Stuttgart (HLRS), on the ARA cluster at Friedrich Schiller University Jena, and on the supercomputer SuperMUC-NG at the Leibniz-Rechenzentrum (LRZ [89]) Munich. The ARA cluster is funded in part by DFG Grants No. INST 275/334-1 FUGG and No. INST 275/363-1 FUGG, and ERC Starting Grant, Grant Agreement No. BinGraSp-714626. The authors acknowledge HLRS for funding this project by providing access to the supercomputer HPE Apollo Hawk under the Grant No. INTRHYGUE/44215. The authors acknowledge also the Gauss Centre for Supercomputing e.V. [90] for funding this project by providing computing time to the GCS Supercomputer SuperMUC-NG at LRZ (allocation pn68wi).

APPENDIX A: PUNCTURE TRACKS AND ψ_4

In this appendix we gather the unprocessed data for ψ_4 extracted at $R = 100M$ and the corresponding puncture trajectories for all simulations. This information is collected in Fig. 11.

APPENDIX B: NR TECHNICAL INFORMATION

1. Code comparison for ψ_4

This appendix shows the comparison between the leading modes of ψ_4 obtained from Einstein Toolkit and GR-Athena++ simulations *without* using extrapolation. Note that this is the data obtained directly from our numerics, so this is a direct comparison between both codes. We write the leading mode of ψ_4 in terms of its phase and shift by

$$\psi_4(t) = a(t)e^{i\tilde{\phi}(t)}. \tag{B1}$$

We show our results for the differences in Fig. 12, and gather the results for the differences at merger in Table VI.

APPENDIX C: IMPACT OF HIGHER MODES

As mentioned in the main text, in this work we are only informing the EOB code with NR information from the leading (2,2) mode. However, even in the absence of NR information, we see that the version of TEOBResumS-Dalì used here is able to describe some of the subleading modes correctly, see Fig. 6.

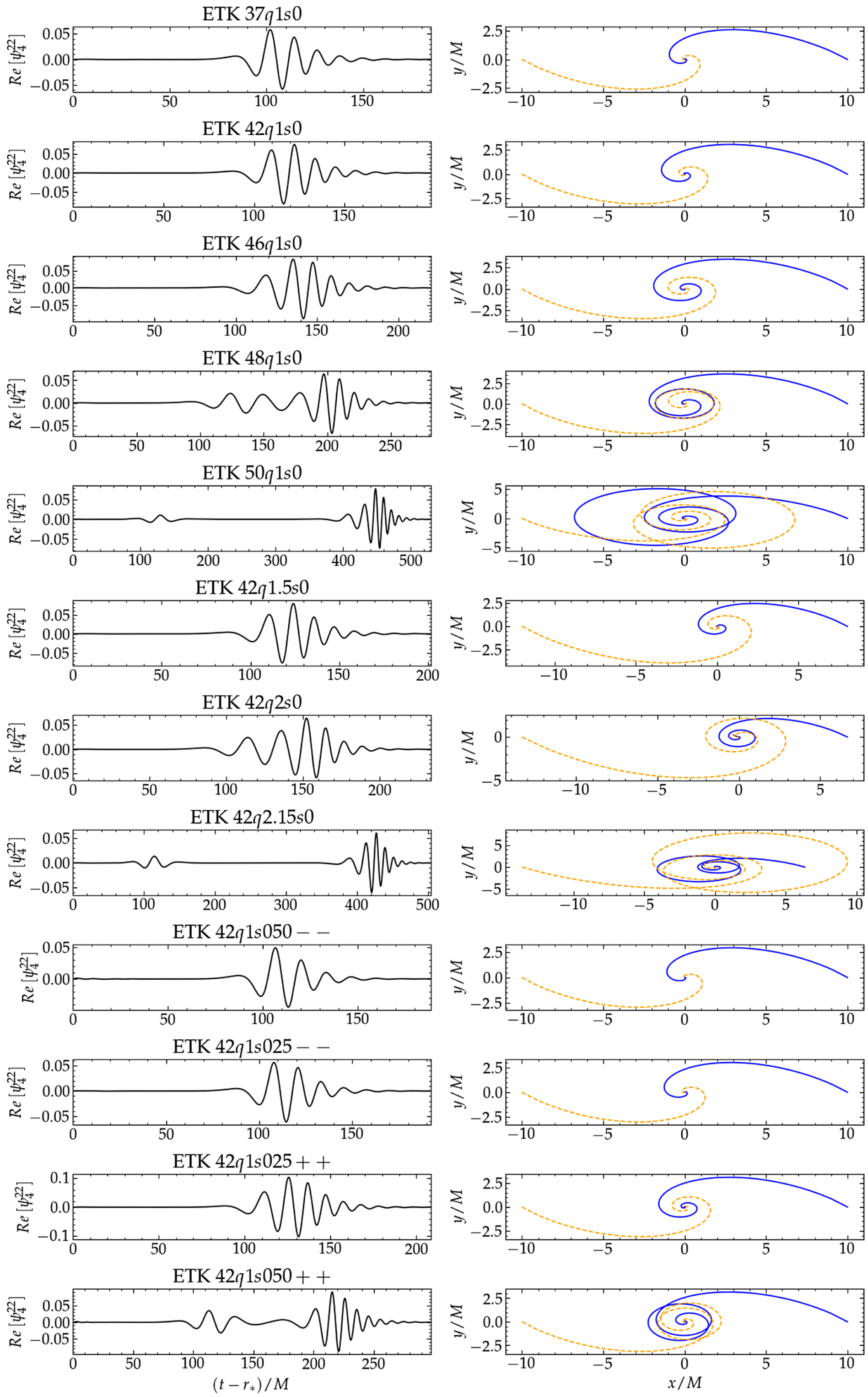

FIG. 11. Puncture tracks and $\psi_4^{(2,2)}$ for all Einstein Toolkit simulations.

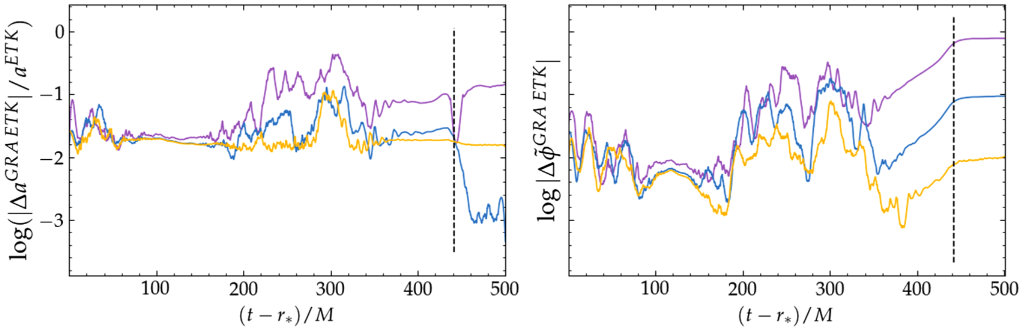

FIG. 12. Comparison between Einstein Toolkit and GR-Athena++ simulations `ETK50` and `GRA50` at fixed resolution. We display the absolute value of the difference in normalized amplitude and phase of the nonextrapolated ψ_4 for every available resolution.

Here we assess the impact of higher modes on EOB/NR comparisons, by computing the contribution of the (uninformed) subleading EOB modes to the total strain via Eq. (2). More precisely, we compute the EOB and NR strain using the leading (2,2) modes only, and compare the results to those obtained using the set $\{(2,2),(2,1),(3,3),(3,2),(4,4),(5,5)\}$. In both cases, we compute the EOB/NR unfaithfulness for all of our configurations, see Fig. 13. We note that while the average unfaithfulness slightly increases after the inclusion of higher modes, most values remain below 0.01. The exception is the simulation `ETK37q1s0`, which is the one with smallest angular momentum.

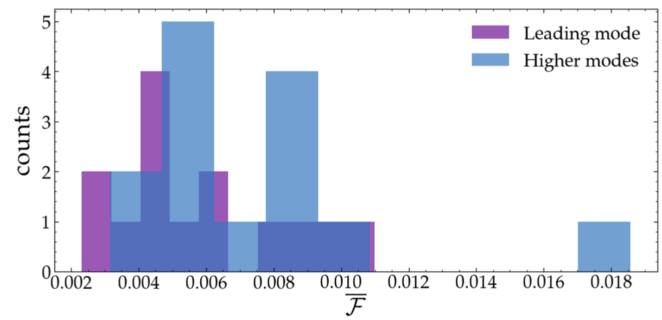

FIG. 13. EOB/NR unfaithfulness in zero noise for all configurations considered. We contrast the results for the strain computed from the leading mode only, and the strain including the modes $\{(2,2),(2,1),(3,3),(3,2),(4,4),(5,5)\}$. We consider an angular orientation with $\theta=\pi/3$, $\phi=0$. The highest value for the unfaithfulness including subleading modes corresponds to the simulation `ETK37q1s0`.

APPENDIX D: EVIDENCE OF UNBOUNDED CONFIGURATIONS

As discussed in the main text, our NR simulations possess $E_0^{\rm ADM}\lesssim M$. In this strict sense, they are bounded configurations with high eccentricity. In this appendix we provide evidence for the interpretation of our NR configurations as the late stages of unbounded orbits, i.e. configurations with initial energy larger than the total mass.

TABLE VI. Amplitude and phase differences at merger for the leading mode of ψ_4 in simulations `ETK42q1s0, 48q1s0, 50q1s0, GRA42q1s0, 48q1s0, 50q1s0` carried out at low, medium, and high resolutions, as listed in Table II.

ID	Resolution	$\Delta a^{\rm GRAETK}_{\rm mrg}/a^{\rm ETK}$	$\Delta\tilde{\phi}^{\rm GRAETK}_{\rm mrg}$
`42q1s0`	L	9.610×10^{-3}	2.179×10^{-2}
	M	1.612×10^{-2}	1.833×10^{-2}
	H	1.728×10^{-2}	1.535×10^{-2}
`48q1s0`	L	1.826×10^{-2}	1.592×10^{-1}
	M	1.963×10^{-2}	2.253×10^{-2}
	H	1.834×10^{-2}	5.373×10^{-3}
`50q1s0`	L	1.817×10^{-2}	6.526×10^{-1}
	M	1.791×10^{-2}	7.651×10^{-2}
	H	1.761×10^{-2}	7.139×10^{-3}

TABLE VII. Comparison between our NR waveforms and EOB waveforms initialized from $r_{\rm EOB}=300M$. From left to right the columns report: the configuration name matching the nomenclature of Table I; the initial EOB energy, the initial EOB angular momentum, and the unfaithfulness between the 22 modes of the NR and EOB waveforms. The unfaithfulness is computed without introducing the NR information in the EOB waveforms.

No.	ID	$E_{\rm EOB}/M$	$J_{\rm EOB}/M^2$	$\bar{\mathcal{F}}_{\rm EOBNR}$
1	`ETK37q1s0`	1.00031	0.87650	0.01968
2	`ETK42q1s0`	1.00028	0.91382	0.02788
3	`ETK44q1s0`	1.00568	1.00213	0.02630
4	`ETK46q1s0`	1.00370	0.99966	0.01196
5	`ETK48q1s0`	1.00388	1.05241	0.01857
6	`ETK50q1s0`	1.00151	1.05059	0.02261
7	`ETK42q1s025-`	1.00027	0.81585	0.01681
8	`ETK42q1s025++`	1.00524	1.07321	0.01671
9	`ETK42q1s050-`	1.00042	0.71710	0.01155
10	`ETK42q1s050++`	1.00054	1.15513	0.00400
11	`ETK42q1s050+-`	1.00049	0.91564	0.02840
12	`ETK42q1.5s0`	1.00583	0.96411	0.02855
13	`ETK42q2s0`	1.00533	0.91745	0.00805
14	`ETK42q2.15s0`	1.00235	0.88935	0.01027

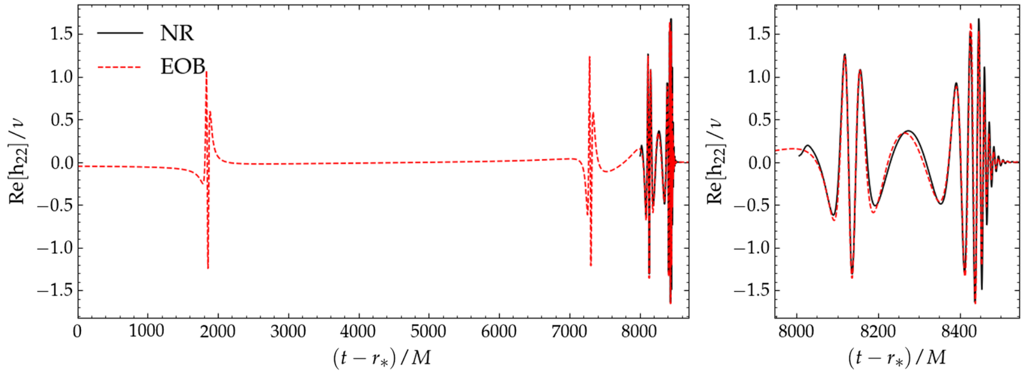

FIG. 14. Comparison between the NR configuration ETK50q1s0 and the corresponding EOB configuration initialized at $r_{\mathrm{EOB}} = 300M$. We display the real parts of the 22 modes for each waveform, enlarging the region covered by the NR simulation on the right panel.

This supports the claim that they truly describe dynamical captures of black holes.

To do this, we match the NR waveforms (which have initial puncture separation $D = 20M$) to EOB configurations initialized at a much larger separation $r_{\mathrm{EOB}} = 300M$. We achieve this by fixing $\Delta r_{\mathrm{EOB}} = 280M$ and optimizing the energy and angular momentum differentials ΔE_{EOB} and ΔJ_{EOB}, as defined in (20)–(22). For all of our configurations, this procedure yields much longer signals, and initial EOB energies larger than M, $E_{\mathrm{EOB}} = E_0^{\mathrm{ADM}} + \Delta E_{\mathrm{EOB}} > M$, see Table VII. In most cases, the EOB waveforms display extra previous encounters with respect to the NR waveforms, see Fig. 14 for a selected example where we show the obtained waveform for ETK50q1s0. We expect we can reproduce the

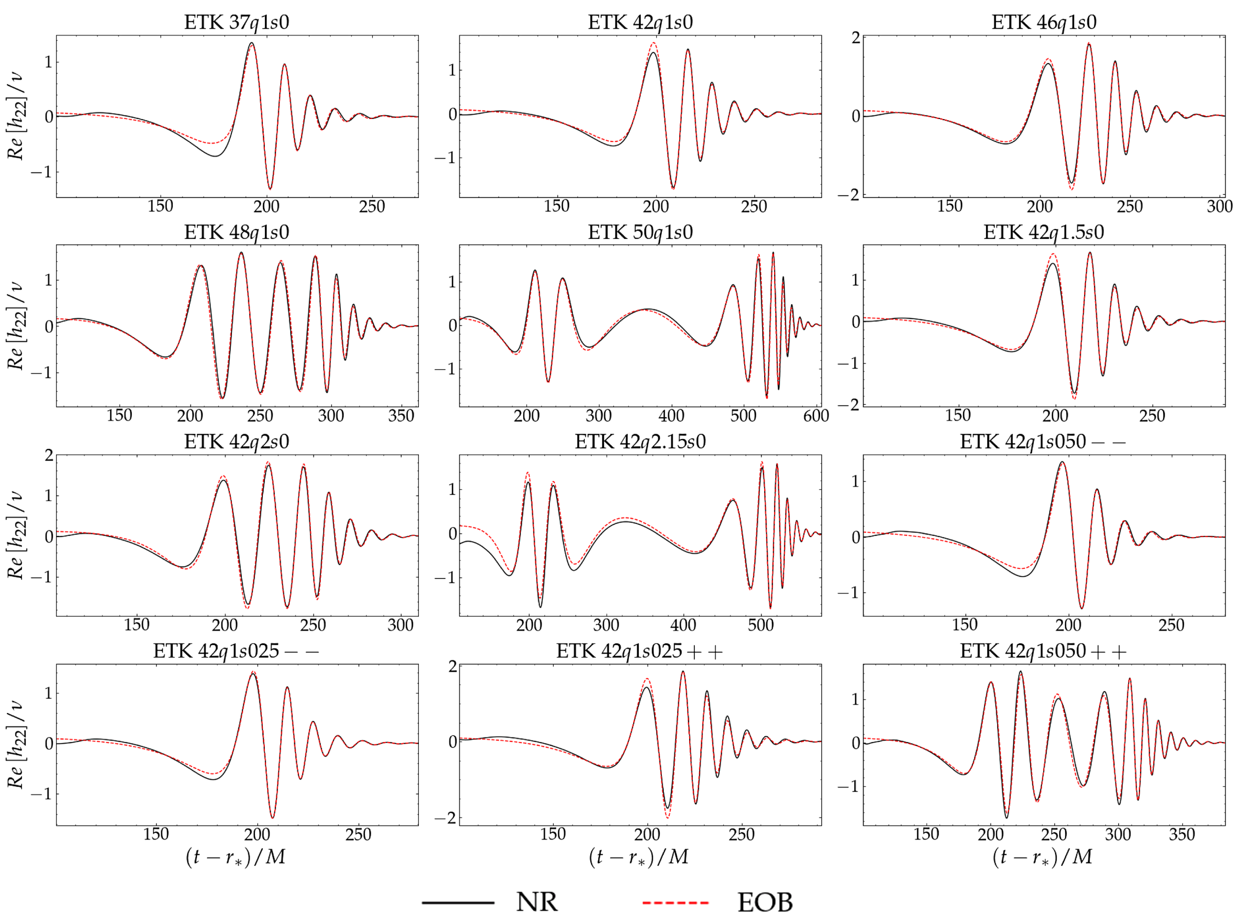

FIG. 15. EOB/NR comparison plots for the real parts of the waveforms for the leading (2, 2) modes, normalized by ν. In the EOB case, we plot the fully NR-informed model, including ringdown and NQC parameters.

same phenomenology using NR configurations with larger puncture separations and initial ADM energies. We leave this for future work.

APPENDIX E: EXTRA EOB/NR PLOTS

In this appendix we gather plots for the EOB/NR comparisons for the leading modes of the strain for all of our Einstein Toolkit simulations. The EOB model includes all of the NR information discussed in the main text, i.e. ringdown, and NQC corrections. We show our results for the real part of h in 15, the modes frequencies in Fig. 16, and the binding energy versus dimensionless angular momentum in Fig. 17.

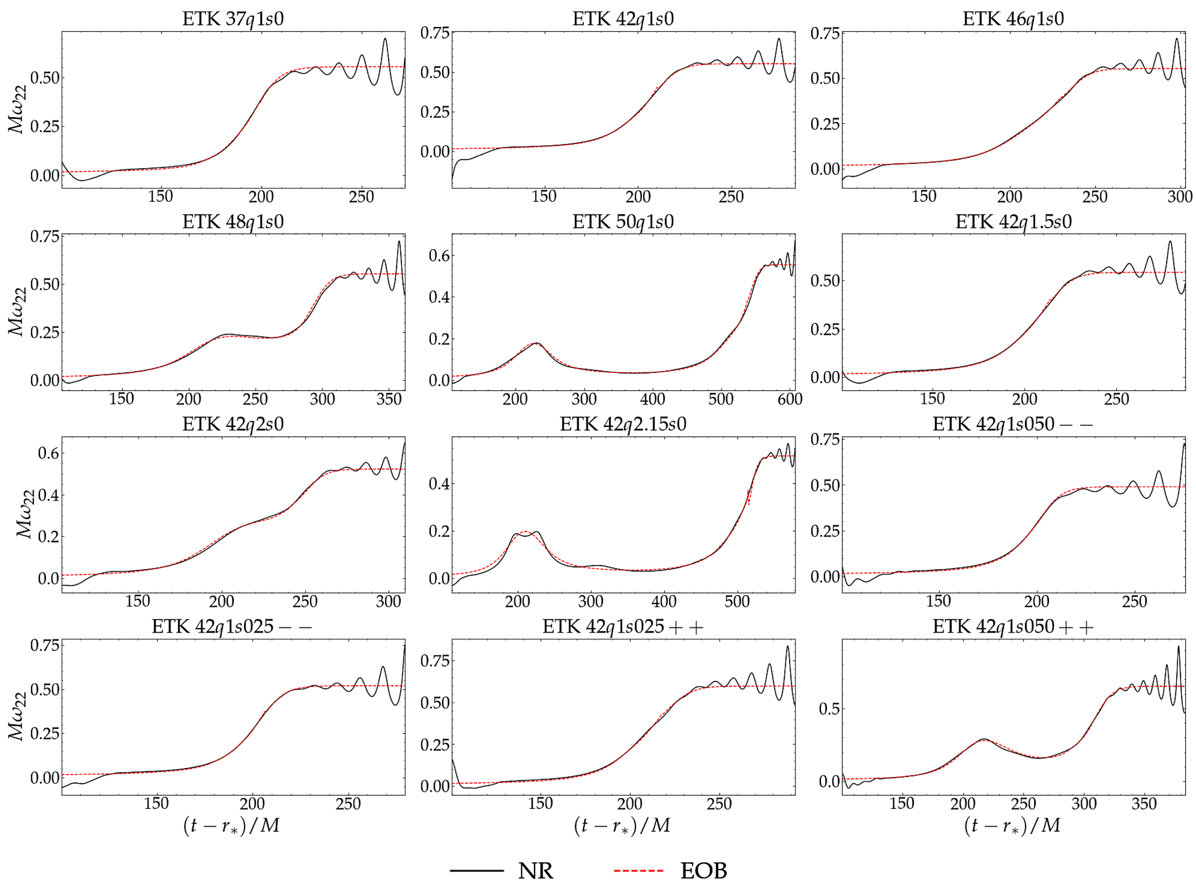

FIG. 16. EOB/NR comparison plots for the frequency of the leading (2, 2) modes. In the EOB case, we plot the fully NR-informed model, including ringdown and NQC parameters.

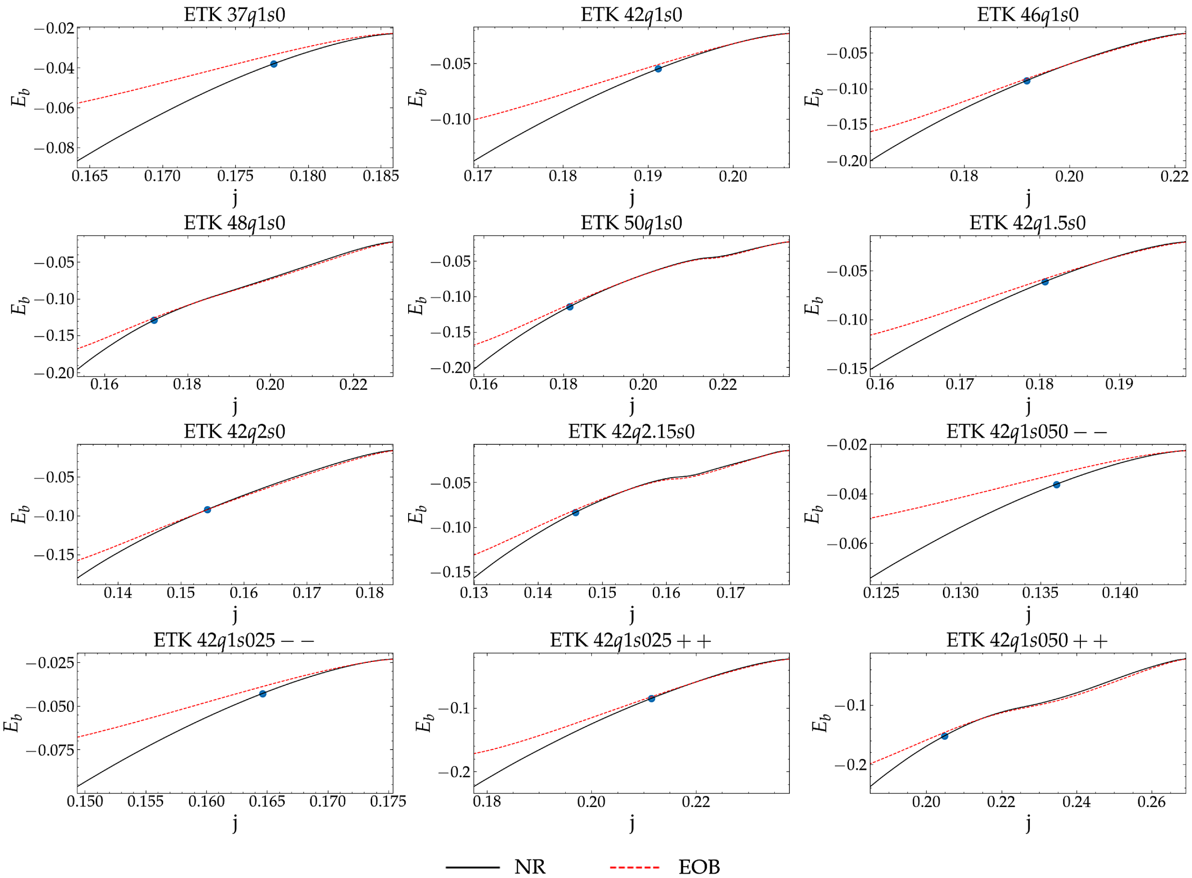

FIG. 17. Binding energy versus dimensionless angular momentum curves for all simulations. The blue marker denotes the NR merger value for each dataset.

[1] J. Aasi et al. (LIGO Scientific Collaboration), Classical Quantum Gravity **32**, 074001 (2015).

[2] F. Acernese et al. (Virgo Collaboration), Classical Quantum Gravity **32**, 024001 (2015).

[3] T. Akutsu et al. (KAGRA Collaboration), Prog. Theor. Exp. Phys. **2021**, 05A101 (2021).

[4] R. Abbott et al. (LIGO Scientific, Virgo, and KAGRA Collaborations), Phys. Rev. X **13**, 041039 (2023).

[5] R. Abbott et al. (LIGO Scientific and Virgo Collaborations), Phys. Rev. Lett. **125**, 101102 (2020).

[6] R. Abbott et al. (LIGO Scientific and Virgo Collaborations), Astrophys. J. Lett. **900**, L13 (2020).

[7] R. Gamba, M. Breschi, G. Carullo, S. Albanesi, P. Rettegno, S. Bernuzzi, and A. Nagar, Nat. Astron. **7**, 11 (2023).

[8] I. M. Romero-Shaw, P. D. Lasky, E. Thrane, and J. C. Bustillo, Astrophys. J. Lett. **903**, L5 (2020).

[9] J. C. Bustillo, N. Sanchis-Gual, A. Torres-Forné, J. A. Font, A. Vajpeyi, R. Smith, C. Herdeiro, E. Radu, and S. H. W. Leong, Phys. Rev. Lett. **126**, 081101 (2021).

[10] V. Gayathri, J. Healy, J. Lange, B. O'Brien, M. Szczepanczyk, I. Bartos, M. Campanelli, S. Klimenko, C. O. Lousto, and R. O'Shaughnessy, Nat. Astron. **6**, 344 (2022).

[11] M. Shibata, K. Kiuchi, S. Fujibayashi, and Y. Sekiguchi, Phys. Rev. D **103**, 063037 (2021).

[12] A. Rasskazov and B. Kocsis, Astrophys. J. **881**, 20 (2019).

[13] H. Tagawa, Z. Haiman, and B. Kocsis, Astrophys. J. **898**, 25 (2020).

[14] M. Zevin, J. Samsing, C. Rodriguez, C.-J. Haster, and E. Ramirez-Ruiz, Astrophys. J. **871**, 91 (2019).

[15] J. Samsing and D. J. D'Orazio, Mon. Not. R. Astron. Soc. **481**, 5445 (2018).

[16] A. Nagar, P. Rettegno, R. Gamba, and S. Bernuzzi, Phys. Rev. D **103**, 064013 (2021).

[17] W. E. East, S. T. McWilliams, J. Levin, and F. Pretorius, Phys. Rev. D **87**, 043004 (2013).

[18] N. Loutrel, arXiv:2009.11332.

[19] R. M. O'Leary, B. Kocsis, and A. Loeb, Mon. Not. R. Astron. Soc. **395**, 2127 (2009).

[20] P. Amaro-Seoane, Phys. Rev. D **98**, 063018 (2018).
[21] M. Punturo, M. Abernathy, F. Acernese, B. Allen, N. Andersson *et al.*, Classical Quantum Gravity **27**, 084007 (2010).
[22] S. Mukherjee, S. Mitra, and S. Chatterjee, Mon. Not. R. Astron. Soc. **508**, 5064 (2021).
[23] R. Gold and B. Brügmann, Phys. Rev. D **88**, 064051 (2013).
[24] P. E. Nelson, Z. B. Etienne, S. T. McWilliams, and V. Nguyen, Phys. Rev. D **100**, 124045 (2019).
[25] Y.-B. Bae, H. M. Lee, and G. Kang, Astrophys. J. **900**, 175 (2020).
[26] S. Jaraba and J. Garcia-Bellido, Phys. Dark Universe **34**, 100882 (2021).
[27] J. Healy and C. O. Lousto, Phys. Rev. D **105**, 124010 (2022).
[28] T. Damour and A. Nagar, Phys. Rev. D **90**, 024054 (2014).
[29] S. Bernuzzi, A. Nagar, T. Dietrich, and T. Damour, Phys. Rev. Lett. **114**, 161103 (2015).
[30] A. Nagar, G. Riemenschneider, and G. Pratten, Phys. Rev. D **96**, 084045 (2017).
[31] A. Nagar *et al.*, Phys. Rev. D **98**, 104052 (2018).
[32] S. Akcay, S. Bernuzzi, F. Messina, A. Nagar, N. Ortiz, and P. Rettegno, Phys. Rev. D **99**, 044051 (2019).
[33] A. Nagar, G. Pratten, G. Riemenschneider, and R. Gamba, Phys. Rev. D **101**, 024041 (2020).
[34] A. Nagar, G. Riemenschneider, G. Pratten, P. Rettegno, and F. Messina, Phys. Rev. D **102**, 024077 (2020).
[35] D. Chiaramello and A. Nagar, Phys. Rev. D **101**, 101501 (2020).
[36] A. Nagar, A. Bonino, and P. Rettegno, Phys. Rev. D **103**, 104021 (2021).
[37] A. Nagar and P. Rettegno, Phys. Rev. D **104**, 104004 (2021).
[38] H. L. Iglesias *et al.*, arXiv:2208.01766.
[39] T. Damour, F. Guercilena, I. Hinder, S. Hopper, A. Nagar, and L. Rezzolla, Phys. Rev. D **89**, 081503 (2014).
[40] S. Hopper, A. Nagar, and P. Rettegno, Phys. Rev. D **107**, 124034 (2023).
[41] T. Damour and P. Rettegno, Phys. Rev. D **107**, 064051 (2023).
[42] A. Albertini, A. Nagar, P. Rettegno, S. Albanesi, and R. Gamba, Phys. Rev. D **105**, 084025 (2022).
[43] A. Albertini, A. Nagar, A. Pound, N. Warburton, B. Wardell, L. Durkan, and J. Miller, Phys. Rev. D **106**, 084061 (2022).
[44] A. Albertini, A. Nagar, A. Pound, N. Warburton, B. Wardell, L. Durkan, and J. Miller, Phys. Rev. D **106**, 084062 (2022).
[45] S. Albanesi, A. Nagar, and S. Bernuzzi, Phys. Rev. D **104**, 024067 (2021).
[46] S. Albanesi, A. Nagar, S. Bernuzzi, A. Placidi, and M. Orselli, Phys. Rev. D **105**, 104031 (2022).
[47] G. Morrás, J. García-Bellido, and S. Nesseris, Phys. Dark Universe **35**, 100932 (2022).
[48] M. Ebersold, S. Tiwari, L. Smith, Y.-B. Bae, G. Kang, D. Williams, A. Gopakumar, I. S. Heng, and M. Haney, Phys. Rev. D **106**, 104014 (2022).
[49] F. Löffler *et al.*, Classical Quantum Gravity **29**, 115001 (2012).
[50] S. Brandt and B. Brügmann, Phys. Rev. Lett. **78**, 3606 (1997).
[51] M. Ansorg, B. Brügmann, and W. Tichy, Phys. Rev. D **70**, 064011 (2004).
[52] T. W. Baumgarte and S. L. Shapiro, Phys. Rev. D **59**, 024007 (1999).
[53] M. Shibata and T. Nakamura, Phys. Rev. D **52**, 5428 (1995).
[54] B. Daszuta, F. Zappa, W. Cook, D. Radice, S. Bernuzzi, and V. Morozova, Astrophys. J. Suppl. Ser. **257**, 25 (2021).
[55] C. Bona, T. Ledvinka, C. Palenzuela, and M. Zacek, Phys. Rev. D **67**, 104005 (2003).
[56] F. Pretorius and D. Khurana, Classical Quantum Gravity **24**, S83 (2007).
[57] C. O. Lousto, H. Nakano, Y. Zlochower, and M. Campanelli, Phys. Rev. D **82**, 104057 (2010).
[58] H. Nakano, Classical Quantum Gravity **32**, 177002 (2015).
[59] C. Reisswig and D. Pollney, Classical Quantum Gravity **28**, 195015 (2011).
[60] T. Damour, A. Nagar, D. Pollney, and C. Reisswig, Phys. Rev. Lett. **108**, 131101 (2012).
[61] A. Nagar, T. Damour, C. Reisswig, and D. Pollney, Phys. Rev. D **93**, 044046 (2016).
[62] S. Bernuzzi, A. Nagar, M. Thierfelder, and B. Brügmann, Phys. Rev. D **86**, 044030 (2012).
[63] S. Bernuzzi, T. Dietrich, W. Tichy, and B. Brügmann, Phys. Rev. D **89**, 104021 (2014).
[64] S. Bernuzzi, M. Thierfelder, and B. Brügmann, Phys. Rev. D **85**, 104030 (2012).
[65] B. Brügmann, J. A. Gonzalez, M. Hannam, S. Husa, U. Sperhake, and W. Tichy, Phys. Rev. D **77**, 024027 (2008).
[66] G. Riemenschneider, P. Rettegno, M. Breschi, A. Albertini, R. Gamba, S. Bernuzzi, and A. Nagar, Phys. Rev. D **104**, 104045 (2021).
[67] A. Buonanno and T. Damour, Phys. Rev. D **59**, 084006 (1999).
[68] A. Buonanno, Y. Chen, and T. Damour, Phys. Rev. D **74**, 104005 (2006).
[69] A. Bonino, R. Gamba, P. Schmidt, A. Nagar, G. Pratten, M. Breschi, P. Rettegno, and S. Bernuzzi, Phys. Rev. D **107**, 064024 (2023).
[70] M. Khalil, A. Buonanno, J. Steinhoff, and J. Vines, Phys. Rev. D **104**, 024046 (2021).
[71] A. Placidi, S. Albanesi, A. Nagar, M. Orselli, S. Bernuzzi, and G. Grignani, Phys. Rev. D **105**, 104030 (2022).
[72] S. Albanesi, A. Placidi, A. Nagar, M. Orselli, and S. Bernuzzi, Phys. Rev. D **105**, L121503 (2022).
[73] E. Berti, V. Cardoso, and C. M. Will, Phys. Rev. D **73**, 064030 (2006).
[74] P. Virtanen *et al.*, Nat. Methods **17**, 261 (2020).
[75] B. Walther, B. Brügmann, and D. Müller, Phys. Rev. D **79**, 124040 (2009).
[76] A. Nitz *et al.*, GWASTRO/PyCBC: v2.0.5 release of PyCBC, 10.5281/zenodo.6912865 (2022).
[77] Updated Advanced LIGO sensitivity design curve, https://dcc.ligo.org/LIGO-T1800044/public.
[78] A. M. Abrahams and R. H. Price, Phys. Rev. D **53**, 1963 (1996).
[79] A. Nagar and L. Rezzolla, Classical Quantum Gravity **22**, R167 (2005).

[80] E. Pazos, E. N. Dorband, A. Nagar, C. Palenzuela, E. Schnetter, and M. Tiglio, Classical Quantum Gravity **24**, S341 (2007).
[81] A. Buonanno, Y. Pan, H. P. Pfeiffer, M. A. Scheel, L. T. Buchman, and L. E. Kidder, Phys. Rev. D **79**, 124028 (2009).
[82] N. T. Bishop, C. Reisswig, D. Pollney, and B. Szilagyi, in *12th Marcel Grossmann Meeting on General Relativity* (World Scientific, Singapore, 2009), pp. 816–819.
[83] C. Reisswig, N. Bishop, D. Pollney, and B. Szilagyi, Phys. Rev. Lett. **103**, 221101 (2009).
[84] C. Reisswig, N. T. Bishop, D. Pollney, and B. Szilagyi, Classical Quantum Gravity **27**, 075014 (2010).
[85] J. Calderon Bustillo, I. C. F. Wong, N. Sanchis-Gual, S. H. W. Leong, A. Torres-Forne, K. Chandra, J. A. Font, C. Herdeiro, E. Radu, and T. G. F. Li, Phys. Rev. X **13**, 041048 (2023).
[86] S. Ossokine, T. Dietrich, E. Foley, R. Katebi, and G. Lovelace, Phys. Rev. D **98**, 104057 (2018).
[87] https://bitbucket.org/eob_ihes/teobresums/.
[88] https://www.uv.es/uvweb/servei-informatica/ca/serveis/investigacio/calcul-cientific-universitat-1286033621557.html.
[89] https://www.lrz.de.
[90] https://www.gauss-centre.eu.